The Astrophysical Journal, 919:40 (25pp), 2021 September 20 https://doi.org/10.3847/1538-4357/ac1070

The Highly Self-absorbed Blazar PKS 1351-018

Brian Punsly[1,2,3], Sándor Frey[4,5], Cormac Reynolds[6], Paola Marziani[7], Alexander Pushkarev[8,9], Sina Chen[10], Shang Li[11], and Preeti Kharb[12]
[1] 1415 Granvia Altamira, Palos Verdes Estates, CA 90274, USA; brian.punsly@cox.net
[2] ICRANet, Piazza della Repubblica 10 Pescara I-65100, Italy
[3] ICRA, Physics Department, University La Sapienza, Roma, Italy
[4] Konkoly Observatory, ELKH Research Centre for Astronomy and Earth Sciences, Konkoly Thege Miklós út 15-17, 1121 Budapest, Hungary
[5] Institute of Physics, ELTE Eötvös Loránd University, Pázmány Péter sétány 1/A, 1117 Budapest, Hungary
[6] CSIRO Astronomy and Space Science, P.O. Box 1130, Bentley WA 6102, Australia
[7] INAF, Osservatorio Astronomico di Padova, Italy
[8] Crimean Astrophysical Observatory, Nauchny 298409, Crimea†, Russia
[9] Astro Space Center of Lebedev Physical Institute, Profsoyuznaya 84/32, Moscow 117997, Russia
[10] Physics Department, Technion Haifa, 32000, Israel
[11] School of Physics and Materials Science, Anhui University, Hefei 230601, People's Republic of China
[12] National Centre for Radio Astrophysics, Tata Institute of Fundamental Research, Post Bag 3, Ganeshkhind, Pune 411007, India
Received 2021 April 27; revised 2021 June 9; accepted 2021 June 29; published 2021 September 22

Abstract

PKS 1351-018 at a redshift of $z = 3.71$ is one of the most luminous, steady synchrotron sources with a luminosity $>10^{47}$ erg s^{-1}. The synchrotron luminosity does not seem to have varied by more than ∼25% over 35 yr. In order to appreciate this remarkable behavior, if it were at $z = 0.5$, it would have a flux density at 15 GHz in a range of 110–137 Jy over 11 yr. In spite of this steady behavior, two strong γ-ray flares $\lesssim 10^{49}$ erg s^{-1} were detected in 2011 and 2016. There is a blazar-like behavior coexisting with the steady behavior. This study is aimed at elucidating the dual nature of this source. We find that the radio source is extremely compact with a bright core and a steep spectrum secondary component, 12 mas away, that appears to be constant in position and flux density in six epochs from 1995–2018. We estimate that a jet with a time averaged power of $(5.2 \pm 3.2) \times 10^{45}$ erg s^{-1} terminates in this lobe, which is advancing $\gtrsim 0.9c$ at a deprojected distance of 1–3 kpc from the central engine. This is the rare case of a young (∼6000 yr), very powerful radio source that is viewed a few degrees from the jet axis. We find evidence of a high velocity (4000 km s^{-1}), high ionization wind emanating from a luminous quasar. The young radio jet appears to experience modest bending as it navigates through the intense quasar environment.

Unified Astronomy Thesaurus concepts: Radio loud quasars (1349)

1. Introduction

The quasar PKS 1351-018 was identified as one of the most luminous of the known *ultraluminous radio cores* with a synchrotron luminosity of $>10^{47}$ erg s^{-1} (Punsly 1995). This is a high redshift quasar at $z = 3.71$ (Osmer et al. 1994). The flux density decreases sharply at frequencies below 6.5 GHz in the quasar rest frame (Spoelstra et al. 1985). Thus, at one time, it was considered a candidate gigahertz peaked spectrum (GPS) radio source with an observed spectral peak near 1.4 GHz (Spoelstra et al. 1985; O'Dea et al. 1991). In spite of the spectral turnover below 6.5 GHz, it was later rejected as a GPS quasar due to the broad spectral peak (de Vries et al. 1997). PKS 1351-018 also has a steady spectrum based on the twenty-one 5.0 GHz (23.5 GHz in the quasar rest frame) flux density measurements from the Australia Telescope Compact Array (ATCA) calibrator webpage[13] over a 15 yr period. The mean flux density is 930 mJy with a standard deviation of 43 mJy. The measured data variation of ±4.7% is similar to the 5% uncertainty that is estimated for individual ATCA flux density measurements (Murphy et al. 2010). Similarly, but statistically less significant, there are eight 22.4 GHz (106 GHz in the quasar rest frame) ATCA calibrator observations over 11 yr with a mean of 543 mJy and a standard deviation of 35 mJy or 6.5%. In spite of this steady behavior, PKS 1351-018 was detected in γ-rays by the Large Area Telescope (LAT) on board the Fermi satellite (Ackermann et al. 2017; Li et al. 2018; Sahakyan et al. 2020). It is this dichotomy, a steady behavior near the spectral peak at centimeter wavelengths and the extreme blazar-like strong γ-ray flares and enormous synchrotron luminosity, that has motivated the following detailed study of this extremely powerful jet source in the early universe.

The paper begins with an in-depth study of the radio light curves to look for evidence of blazar-like phenomenon in Section 2. In Section 3, we consider radio interferometer imaging in order to look for blazar-like structure changes and to define the source size. In Section 4, we construct the synchrotron spectral energy distribution (SED). We analyze the optical spectrum and use it to define the energetics of the accretion flow in Section 5. We follow this up with a depiction of the γ-ray flares (Section 6). In Sections 7 and 8, we develop simple models of the stationary secondary component at ∼12.5 mas from the nucleus. We are then able to bound the jet power. Throughout this paper, we adopt the following cosmological parameters: $H_0 = 69.6$ km s^{-1} Mpc^{-1}, $\Omega_\Lambda = 0.714$, and $\Omega_m = 0.286$, and use Ned Wright's Javascript Cosmology Calculator website (Wright 2006). In our adopted cosmology we use a conversion of 7.31 pc to 1 mas.

2. 5 GHz Light-curve Analysis

Light curves can indicate evidence of blazar-like behavior. Rapid variations can be used to estimate the brightness

† While the AAS journals adhere to and respect UN resolutions regarding the designations of territories (available at http://www.un.org/press/en), it is our policy to use the affiliations provided by our authors on published articles.
[13] http://www.narrabri.atnf.csiro.au/calibrators/

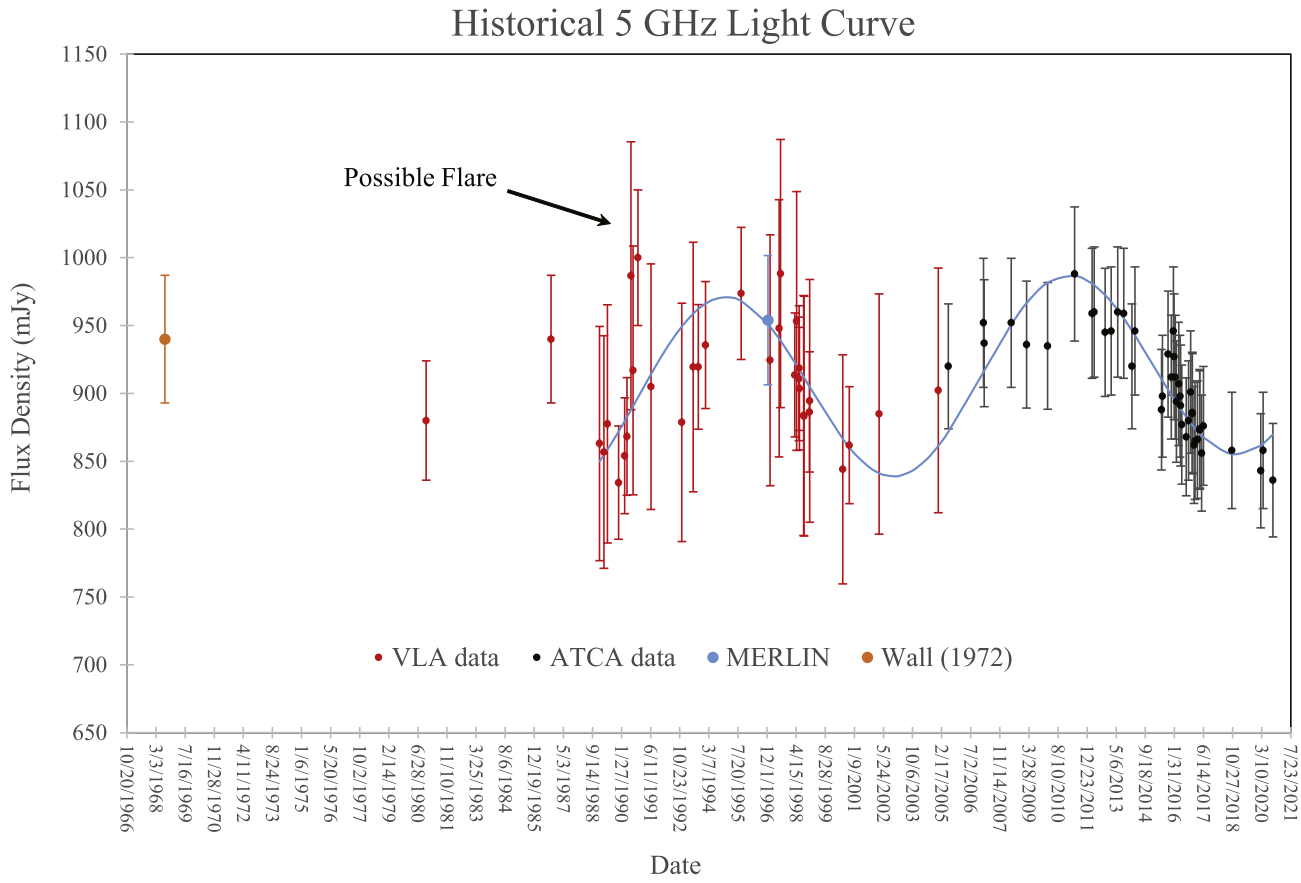

Figure 1. The highest density time sampling at any radio frequency is obtained at 5 GHz. The light curve is essentially in two halves, one is based primarily on VLA data and the latter half is based on ATCA data. This eliminates any perceived short term variability that is a consequence of absolute flux density calibration scales from different telescopes. We have verified in multiple epochs that the VLA flux density is consistently lower than the quasi-simultaneous ATCA flux density. There is a slow gradual variation that is visually highlighted by a sine curve with no physical meaning or statistical significance ascribed to it—only for a visual aid. There is also a sign of a flare in 1990. Flares are difficult to verify since the measurement uncertainty is large enough to be consistent with enormous intrinsic flux density changes at this very high redshift. The MERLIN observation is described in Section 3.

temperature, T_b. Figure 1 shows the most densely sampled radio light curve that we could create. There are more archival data at 5 GHz (corresponding to 23.5 GHz in the quasar rest frame) than at other frequencies. If there is a blazar coexisting with strong, persistent emission, it can be significantly variable at higher frequency such as 1.25 cm wavelength in the quasar rest frame (Tornikoski et al. 2001). Figure 1 illustrates the difficulties associated with the analysis. PKS 1351-018 has modest variation on the order of 5%–10% of the background of a quiescent flux density of ∼900 mJy. Yet, the uncertainty in the individual observations is 5%–10%. The data for Figure 1 can be found in Appendix A.

In order to get access to a large volume of unpublished Very Large Array (VLA) data (in the time frame before ATCA data became available), we relied on the National Radio Astronomy Observatory (NRAO) VLA Archive Survey (NVAS) Images Pilot page.[14] We downloaded calibrated visibility FITS files and performed a self-calibration of the phase. This is a bright source with no confusing nearby sources, which lends itself to successful self-calibration. In general, we do not know the history of these data sets, for instance, the observer's intent with respect to the science goals and the flux density accuracy goal or if accurate automated *bad data flagging* was implemented properly. For outlier data points (candidates for rapid change), we considered things such as image rms noise, signatures of phase noise or side lobes in the images of this unresolved source and elevation above the horizon. For crucial, suspect data sets, we had to reduce the data by hand and flag bad antennas and reprocess the images. In order to minimize these issues we chose to avoid early VLA images that were not already present in the literature. In the end, the most conservative flux density calibration uncertainty that we can choose is 10% in general (Lorant Sjouwerman[15], private communication). Although looking at the scatter of the points, this might be too large for most observations. However, if we were able to ascertain (i.e., from published papers or direct contact with the principal investigator) that the data reduction proceeded without these potential issues, an uncertainty in the flux density measurements is 5% based on the VLA manual[16] (see also Perley & Butler 2013). We did not find all these circumstances since it is sometimes difficult to recreate the past. This seemed like a reasonable compromise as NVAS FITS files greatly reduce the time required to analyze a large volume of data at the expense of a larger uncertainty.

We also wanted to increase the density of the time sampling of the ATCA observations after 2007. There were numerous

[14] http://archive.nrao.edu/nvas/read.shtml

[15] Contact person for NVAS.

[16] https://science.nrao.edu/facilities/vla/docs/manuals/oss/performance/fdscale

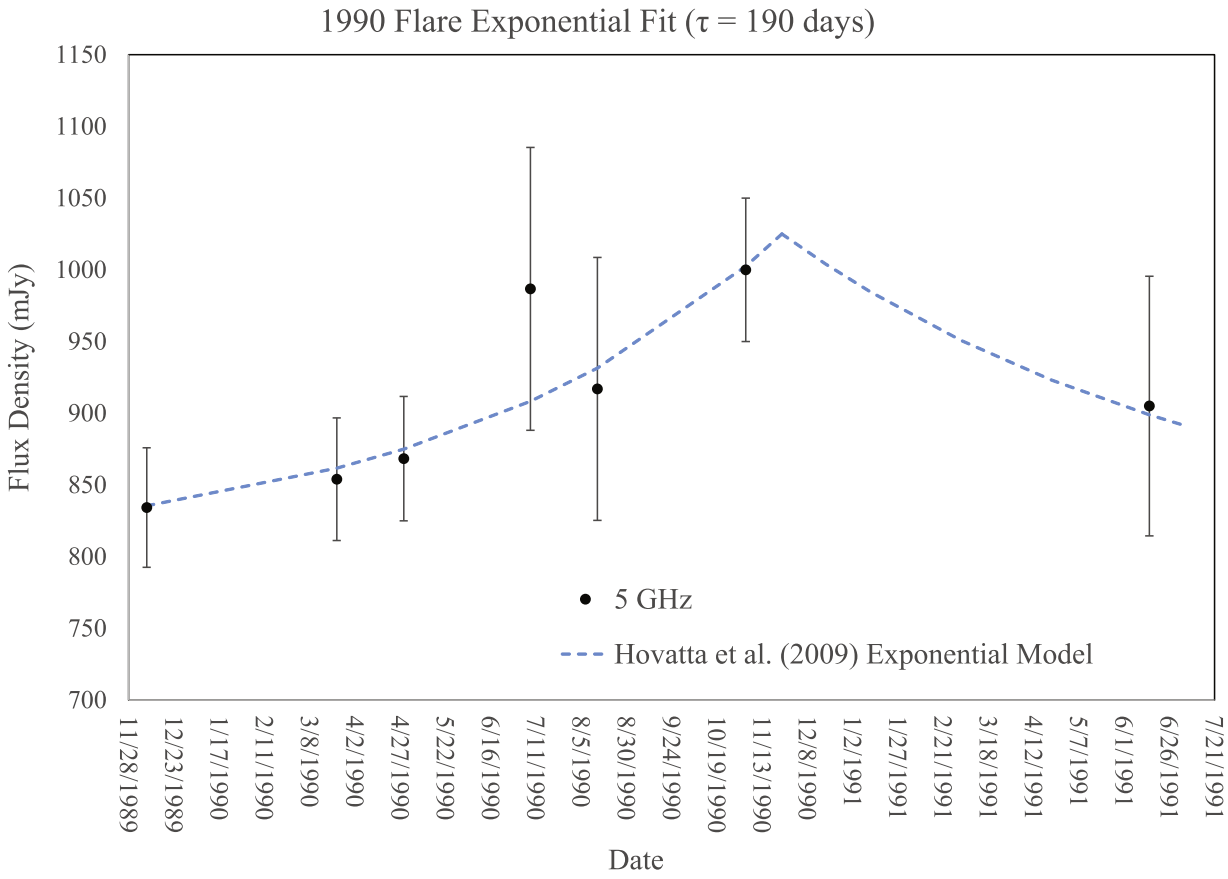

Figure 2. Evidence of a 5 GHz flare is presented in this close-up of the corresponding region in Figure 1. We fit the flux densities with a blazar flare model from the literature that is described in the text.

observations in projects C2898 (2014) and C2914 (2016). The reductions of these data were generously provided for the purposes of this paper by Jamie Stevens (ATCA Senior System Scientist). The dense data sampling highlights the gradual changes in the flux density. This was true even in the summer of 2016 when there was a large γ-ray flare (see Section 6).

With that qualifier on the large VLA uncertainty aside, note that there are not the recurring large abrupt changes in amplitude in Figure 1 that one sometimes observes with a blazar (Tornikoski et al. 2001; Hovatta et al. 2009). But, there is some modest slow variation in amplitude. We have superimposed a sine wave on the densely sampled data from 1988–2020 in order to draw one's eye to the gentle waves of variability that seem to exist within the data set even though the error bars are of similar amplitude. We do not, in any way, suggest that there is periodic behavior. This is only a device to emphasize the subtle long term variations. We can crudely estimate changes (peak to peak) of ~140 mJy over time frames of ~8 yr. This crude estimate is adequate for our purposes. The time variable brightness temperature is estimated in Hovatta et al. (2009) as

$$T_{\rm b} = 1.548 \times 10^{-32} \frac{\Delta S_\nu d_L^2}{\nu^2 t^2 (1+z)}, \quad (1)$$

where ΔS_ν (measured in jansky) is the change in flux density observed at frequency ν (measured in gigahertz) in a time frame t (measured in days in the observer's frame), and d_L is the luminosity distance measured in meters. The slow wave modulation yields $T_{\rm b} = 2.26 \times 10^{12}$ K. When $T_{\rm b} > 10^{12}$ K, the inverse Compton catastrophe occurs. Most of the electron energy is radiated in the inverse Compton regime. The radio synchrotron spectrum from the jet is diminished in intensity to unobservable levels (Kellermann & Pauliny-Toth 1969). In order to explain the observed radio synchrotron jet in such sources, Doppler boosting is customarily invoked to resolve the paradox. The minimum Doppler factor, δ, required to avoid the inverse Compton catastrophe is (Hovatta et al. 2009)

$$\delta > \left[\frac{T_{\rm b}}{10^{12}\ {\rm K}}\right]^{0.33}. \quad (2)$$

We note that slightly smaller values for the denominator ($T_{\rm b} \sim 1$–5×10^{11} K) based on the equipartition assumption are often invoked (Readhead 1994). However, based on component sizes and flux density measured with Very Long Baseline Interferometry (VLBI) we estimate $T_{\rm b} \approx 10^{12}$ K, in the next section on radio images. Furthermore, this paper does not assume equipartition in the jet, as we discuss in Section 8. From Equations (1) and (2), we get a bound of $\delta > 1.31$, not the kind of large Doppler factor expected for a strong γ-ray flare (Sahakyan et al. 2020).

The best evidence for a flare in Figure 1 is the indicated region during 1990. This requires special consideration of the data in order to verify that this sparsely sampled event is not a manifestation of flawed observations or data reductions. We consider a magnified view of this region for a detailed analysis in Figure 2.

Before defining the flare, we noted that the 1990 August 14 data had six antennas for which the gain amplitude did not track the other 20 antennas, for whatever reason. The data were processed by hand by Lorant Sjouwerman instead of the automated NVAS routine. These antennas were flagged and the data reduction repeated based on the other 20 antennas followed by a phase self-calibration. Figure 2 indicates our best estimates of the flux density and uncertainty. We fit this with a blazar flare model developed in Valtaoja et al. (1999) and Hovatta et al. (2009). The authors successfully describe flares by an exponential rise followed by an exponential decay with a time constant 1.3 times the time constant of the rising phase. We fit the data by finding the aforementioned model that minimizes the excess variance, $\Sigma_{\rm rms}$, of the fit to the seven data points that define the flare in Figure 2 (Nandra et al. 1997):

$$\Sigma_{\rm rms}^2 = \frac{1}{N}\sum_{i=1}^{N}\frac{(S_i - f_i)^2 - \sigma_i^2}{f_i^2}, \quad (3)$$

where i labels one of the N measured flux densities, f_i is the expected value of this flux density from the Hovatta et al. (2009) model, S_i is the measured flux density, and σ_i is the uncertainty in this measurement. The best fit is the one that peaks on 1990 November 24 at 1025 mJy, corresponding to a flare peak of 225 mJy above the baseline. The time constant of the rise is $\tau = 190$ days. Hovatta et al. (2009) use $\tau = t$ in Equation 1. They also identify the flare peak (225 mJy in this case) with ΔS_ν in Equation (1). We formally interpret Equation (1) as the change in flux density in a time t. For $t = \tau$, the maximum ΔS_ν during the rise is $\Delta S_\nu = (1 - e^{-1})225\,{\rm mJy} = 142\,{\rm mJy}$. This yields $\delta > 8.1$ from Equation (2).

This minimum value of Doppler factor, $\delta_{\rm min}$, can be used to restrict the line of sight (LOS) to the emitting region of the jet. First, we express the Doppler factor in terms of kinematic quantities,

$$\delta = \frac{\gamma^{-1}}{1 - \beta\cos\theta}, \quad \gamma^{-2} = 1 - \beta^2, \quad (4)$$

where β is the normalized three-velocity of bulk motion, the associated Lorentz factor is γ, and θ is the angle of the motion to the LOS to the observer (Lind & Blandford 1985). For each value of $\delta_{\rm min}$, one can vary β in Equation (4) to find the maximum value of θ, $\theta_{\rm max}\{\delta_{\rm min}[(T_{\rm b})]\}$, that is compatible with $\delta_{\rm min}$ (Ghosh & Punsly 2007):

$$\theta_{\rm max}\{\delta_{\rm min}[(T_{\rm b})]\} = {\rm Max}_{|\beta}\left(\arccos\left\{\left[1 - \left(\frac{\sqrt{1-\beta^2}}{\delta_{\rm min}[(T_{\rm b})]}\right)\right]\beta^{-1}\right\}\right). \quad (5)$$

From the flare model and Equation (5) we conclude that

$$\theta_{\rm max} = 7\overset{\circ}{.}1. \quad (6)$$

Comparing Figures 1 and 2, we draw the following conclusion. There is a blazar-like emission region. However, it is superimposed on the background of a much more luminous mildly variable component. This could be emission from a very luminous sub-kiloparsec scale jet for which δ is far less than in the blazar-like region either due to a strong decelerating force and/or a change in the jet propagation direction relative to the LOS. The analysis of the radio images in the next section can potentially elucidate these circumstances. The apparent lack of many clear instances of blazar-like flares in Figure 1 (only the one in 1990 in Figure 2) is amplified by the time dilation due to the large redshift. In the quasar rest frame, 1989–2020 is only 6.6 yr.

3. Radio Image Analysis

The first radio image that we considered was the 1.4 GHz VLA observation in A-array, which found an unresolved core (Neff & Hutchings 1990). In the absence of diffuse large scale emission we looked for compact structure on kiloparsec scales. First, we imaged the deepest 5 GHz VLA A-array observation, project AB0560 (1990 March 23, one of the data points in Figure 2). Again, it was an unresolved nucleus. We then looked at the most sensitive 5 GHz observation with the Jansky Very Large Array (JVLA) in the A-array, project 16B-130 on 2016 December 3. Matt Smith kindly reduced the data he observed and created an image also showing nothing but an unresolved core. So we went to higher resolution looking for structure, by searching the Multi-Element Radio Linked Interferometer (MERLIN) archives for 5 GHz observations. Anita Richards generously provided the image FITS file of the one observation, on 1996 December 1, revealing an unresolved core. The restoring beam size was 69×52 mas at a position angle PA = 39°. Thus, we have an upper bound on the source size that is quite small. Thus motivated, we explore the VLBI observations of this source to look for the structure on scales less than 50 mas.

3.1. S-band VLBI

The Astrogeo VLBI FITS image database[17] contains calibrated VLBI 2.3 GHz data from numerous epochs from 1994–2020. Most of the observations use the 10 station Very Long Baseline Array (VLBA). However, from 1998–2003, the Research and Development VLBA project employed additionally up to 10 other antennas in order to create a global VLBI network (Petrov et al. 2009; Pushkarev & Kovalev 2012). The addition of the southern hemisphere stations and the multiple short scans in 24 hr long observing sessions provide the best (u, v) coverage and resolution of any of the observations in the Astrogeo VLBI FITS image database. The observation in Figure 3 from 2002 July 24 is of particular interest. The 2.3 GHz image was published in Pushkarev & Kovalev (2012). The 2002 image is the highest sensitivity, high resolution image available at the S band. The visibility data were fit with Gaussian brightness distribution components with an automated process. We reanalyzed the data with a manual data reduction for the purposes of this project. There is a prominent diffuse component to the north (which we will call the *north lobe*). The details of the Gaussian fit are described in the second entry of Table 1. The method of defining measurement uncertainties can be found in Appendix B.

The brightness temperature in the last column is computed per the methods of Kellermann & Owen (1988):

$$T_{\rm b}[{\rm K}] = 1.22 \times 10^{12}(1+z)\frac{S_\nu}{\theta_1\theta_2\nu^2}, \quad (7)$$

where ν is the observed frequency measured in gigahertz, θ_1 (θ_2) is the major (minor) axis of the elliptical Gaussian fitted

[17] http://astrogeo.org

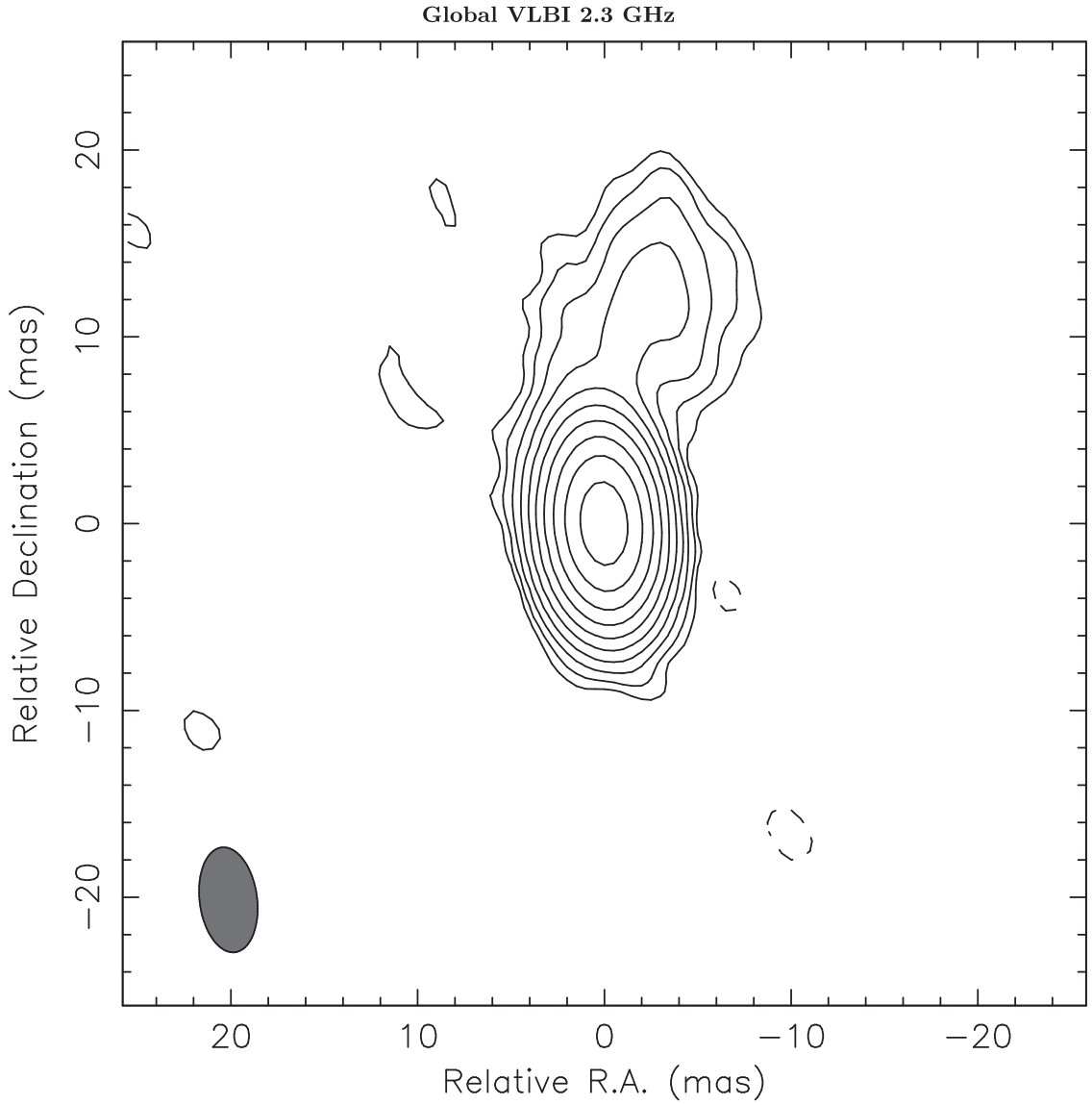

Figure 3. The northern lobe is very important to our estimate of the jet power. The best image of the feature is reconstructed using the *S*-band (2.3 GHz) global VLBI data taken on 2002 July 24. The peak intensity is 718 mJy beam^{-1}. The lowest level contour is ±0.92 mJy beam^{-1} and the positive contour levels increase by a factor of 2. The restoring beam is 3.08 × 5.66 mas at PA = 5°. The lobe appears to be at the end of a short, 11.5 mas jet. The lobe is resolved (fit with a Gaussian of FWHM of 6.6 mas from Table 1). It is comparable to the overall jet length projected on the sky plane. It is also unclear if there is a hot spot. It appears plume-like as opposed to an edge brightened morphology.

FWHM measured in milliarcseconds, and S_ν is the flux density of the component in jansky.

The earliest entry in Table 1 is a VLBA observation from 1997 January 11. It is composed of four 3 minute scans spread out over 2 days to maximize (u, v) coverage. The fits are not carried out to as many decimal points as our other fitted models (Fey & Charlot 2000). The north lobe flux density is 0.03 Jy with no listed uncertainty. Thus, there is an additional uncertainty due to roundoff errors. We also found another image in the Astrogeo VLBI FITS image database with far less dense coverage in the (u, v) plane than the 2002 July 24 image that showed the northern lobe prominently (2014 August 9). The (u, v) coverage was fortuitous and the beam shape is not too elongated as in many epochs. The results of the Gaussian fitting process are listed as the third entry in Table 1. The lobe flux density is probably the same within uncertainty (∼15%–20%), but the smaller component size indicates that some diffuse emission was not captured by the sparse (u, v) coverage. There is strong evidence in Table 1 that the north lobe was stable within VLBI uncertainties for at least 17 yr.

Since these are very high resolution observations, we are interested to know how much flux density outside of the unresolved core was missed by the VLBI observations. In order to assess this and being cognizant of possible temporal variability of the core, we looked for quasi-simultaneous ATCA or VLA observations and VLBI observations. The VLBI absolute flux density calibration is less robust based on comparing the scatter of the *C*-band VLBI flux density to the light curve in Figure 1. Thus, it is very desirable to have two quasi-simultaneous VLBI observations with at least one ATCA or VLA observation at the same epoch. We could not find this circumstance in any of the VLBI bands except for the *S* band. Table 2 shows the only robust comparison that we could make based on archival data.

Table 2 seems to indicate that all of the flux density is contained within the VLBI components of the nucleus and

Table 1
Gaussian Fits to *S*-band VLBI Observations

Date	Component	Flux Density (mJy)	r (mas)	PA (°)	FWHM (mas)	Axial Ratio (PA)	T_b (K)
1997 Jan 11	Core	880 ± 88	0	⋯	1.1	0 (−53°)	8.67×10^{11}
	North lobe	30 ± 13	11.6 ± 1.7	−6	6.1	1	8.76×10^{8}
2002 Jul 24	Core	766 ± 77	0	⋯	1.0	1	8.39×10^{11}
	North lobe	34.5 ± 13.8	11.9 ± 1.1	−9.7	6.6	1	8.50×10^{8}
2014 Aug 9	Core	787 ± 79	0	⋯	1.1	1	7.33×10^{11}
	North lobe	32.6 ± 13.0	12.4 ± 1.7	−11.3	4.8	1	1.54×10^{9}

Table 2
2.3 GHz VLBI Flux Density Compared to ATCA

Date	Telescope	Flux Density (mJy)	Reference
2018 Jan 18	VLBI	970 ± 97[a,b]	Astrogeo VLBI FITS image database
2018 Jan 22	ATCA	893 ± 45[c]	ATCA Calibrator Database
2018 Jan 25	VLBI	923 ± 92[a,b]	Astrogeo VLBI FITS image database
2017 Dec 19[d]	ATCA	881 ± 44[c]	ATCA Calibrator Database

Notes.
[a] The sum of the flux densities of the Gaussian fitted nucleus and the north lobe.
[b] 10% uncertainty (Homan et al. 2002; Pushkarev & Kovalev 2012).
[c] 5% uncertainty (Murphy et al. 2010).
[d] Additional data to corroborate the stability of the ATCA calibration in this time frame.

north lobe. If there were a few milllijansky resolved out of the north lobe by the VLBI observations, we would not be able to confirm or reject this based on the uncertainties of the data in Table 2. We conclude that there is likely no measurable emission between the ∼50 and 60 mas limit from MERLIN and the ∼15 mas VLBI structure. We assume this to be the case in the remainder of the paper, up to the uncertainty in the flux density.

3.2. C-band VLBI

There are more VLBI data at the *C* band than any other frequency band. We were able to find six observations with useful data for our purposes. The relevant details are listed in Table 3. The third column, the restoring beam size, is very important since PKS 1351-018 displays a resolution dependent morphology (Frey et al. 2002). The beam position angle is not listed (to save space for more relevant details) as it is always nearly north–south within 15°. All of the data were fit by us except for the O'Sullivan et al. (2011) data, which is from the literature. We refit the Frey et al. (1997) (u, v) data with circular Gaussian models and multiple nuclear components, so it matches our data reduction technique for the four more recent data that were fit. The models are fit based on four detected components. As in Figure 3, the two most prominent features are the bright nucleus and the diffuse north lobe. There is also a knot in the northern jet (that is prominent in Figure 4) as well as a southeast component that is very close to the nucleus (see Figure 5). The features that are recovered in the fitting process in the (u, v) plane depend on the resolution and sensitivity of the observations.

The main purpose of Table 3 is to track the location of the north lobe over time (Columns 6 and 7). In terms of (u, v) coverage, the four early observations are far superior to the last two from the Astrogeo VLBI FITS image database. Surprisingly the 2014 February 18 Astrogeo observation had much more sensitivity to the north lobe emission than the other two observations from the Astrogeo VLBI FITS image database (see Figure 4). The image is from segment BP177I of the 8th VLBA Calibrator Survey (VCS8) campaign (Petrov 2021). The source was used as an amplitude calibrator and it was observed in one scan on 2014 February 18 and achieved superior dynamic range compared to the other epochs.[18]

Compare the 2001 January 23 VLBI Space Observatory Program (VSOP) observation (Frey et al. 2002) with 10 stations of VLBA plus the Highly Advanced Laboratory for Communications and Astronomy (HALCA) satellite (the second entry in Table 3) restored with natural weighting with the best Astrogeo observation from 2014 February 18 in Figure 4. The north lobe position and flux density is very stable over 13 yr. There is a faint jet connecting the nucleus to the lobe. In the panel on the right, this jet seems to begin at a small brighter protrusion of the nuclear contours almost directly northeast of the core. This is the component *knot in north jet* in Table 3. Based on Table 3 and Figure 4, due to the positional change from 2001–2014, this feature might be different faint knots in 2001 and 2014. The apparent bending of the jet to the east from 2001–2014 might be an indication that there is relativistic motion (Doppler aberration) in this region of the jet.

At higher resolution, at the *C* band, as well as at higher frequency (the next subsection), the diffuse radio emission of the north lobe is resolved out. However, more compact features are revealed. The panel on the left of Figure 5 is from Frey et al. (2002) and represents the same data as in the panel on the left of Figure 4, but a higher resolution image is made using optimally weighted data on space–ground baselines to enhance angular resolution. The north lobe and the knot in the north jet are resolved out, but a *southeast component* is revealed. The absolute flux density calibration with VSOP is difficult, but we estimate ≈40 mJy in the southeast component . In order to validate its

[18] L. Petrov (2021, private communication).

Table 3
Gaussian Fits to *C*-band VLBI Observations

(1) Date	(2) Array/ Frequency	(3) Restoring Beam (mas)	(4) Component	(5) Flux Density (mJy)	(6) r (mas)	(7) Position Angle (°)	(8) FWHM (mas)	(9) Axial Ratio/PA	(10) T_b (K)	(11) Ref.
1995 Jan 28	VLBA 5 GHz	4.9×2.0	Core	919 ± 92	0	⋯	0.57	1	6.50×10^{11}	a,b
			North lobe	14.0 ± 5.6	12.4 ± 0.8	-11.8	2.51	1	5.11×10^{8}	b
			Knot in north jet	Not detected	Not detected	⋯	⋯	⋯	⋯	b
			Southeast component	22.4 ± 7.1	1.6 ± 0.3	131.0	0.05[c]	1	[c]	b,d
2000 Jun 5	Global VLBI 5 GHz	3.51×1.10	Core	681 ± 68	0	⋯	0.77	0.3/ −164°	8.91×10^{11}	e
			North lobe	16.8 ± 6.7	11.9 ± 0.7	-12.9	4.02	1	2.42×10^{8}	
			Knot in north jet	14.3 ± 6.2	1.6 ± 0.3	56.6	[c]	⋯	[c]	
			Southeast component	78.5 ± 14.5	1.0 ± 0.5	132.7	0.48	1	7.88×10^{10}	
2001 Jan23[f]	VSOP 4.8 GHz	3.59×1.60	Core	664 ± 66	0	0	0.46	1	7.83×10^{11}	b,g
			North lobe	14.1 ± 5.6	12.5 ± 0.7	-11.0	3.93	1	2.28×10^{9}	b
			Knot in north jet	4.0 ± 3.0	5.2 ± 0.3	67.0	[c]	⋯	[c]	b
			Southeast component	32.1 ± 8.5	1.3 ± 0.3	113.0	0.05[c]	1	[c]	b
2001 Jan 23[f]	VSOP 4.8 GHz	1.56×0.59	North lobe	Not detected	Not detected	⋯	⋯	⋯	⋯	b
			Southeast component	40 ± 10	1.3 ± 0.3	113.0	[c]	⋯	[c]	b
2014 Feb 18	VLBA 4.3 GHz	3.99×1.59	Core	802 ± 80	0	⋯	0.49	1	1.04×10^{12}	b,h
			North lobe	13.3 ± 5.3	12.6 ± 0.8	-12.4	2.04	1	9.93×10^{9}	b
			Knot in north jet	8.5 ± 4.3	5.7 ± 0.7	18.9	0.68	1	5.71×10^{10}	b
			Southeast component[d]	33.1 ± 8.4	1.4 ± 0.3	106.9	0.01	1	[c,d]	b
2016 Feb 17	VLBA 4.3 GHz	4.08×1.66	Core	656 ± 66	0	⋯	0.55	1	6.27×10^{11}	b,h
			North lobe[i]	9.6 ± 3.8	12.8 ± 0.8	-13.2	1.53	1	[i]	b
			Knot in north jet[d]	7.1 ± 3.3	6.0 ± 0.7	15.6	0.34	1	[c,d]	b
			Southeast component[d]	19.7 ± 5.5	1.5 ± 0.4	114.0	0.04	1	[c,d]	b
2018 Dec 1	VLBA 4.3 GHz	3.81×1.42	Core	699 ± 70	0	⋯	0.46	1	9.76×10^{11}	b,h
			North lobe[i]	11.0 ± 4.4	12.0 ± 0.5	-13.5	1.66	1	[i]	b
			Knot in north jet[d]	13.9 ± 4.9	5.4 ± 0.7	19.1	0.01	1	[c,d]	b
			Southeast component[d]	46.0 ± 9.0	1.4 ± 0.4	118.2	0.06	1	[c,d]	b

Notes.
[a] Frey et al. (1997).
[b] This paper.
[c] Effectively a point source, T_b estimate ill-defined.
[d] Very poor long baseline (u, v) coverage, fit parameters may not be robust.
[e] O'Sullivan et al. (2011).
[f] See the text description of the absolute flux density uncertainty of our results. The second entry for this observation is from the image in Frey et al. (2002) with preferential weighting to the long space–Earth baselines.
[g] Frey et al. (2002).
[h] Petrov (2021), Astrogeo VLBI FITS image database.
[i] (u, v) short baseline coverage is degraded relative to 2014 February 18, much of the north lobe flux density is missing. The true uncertainty cannot be estimated.

existence, we present a global VLBI—VLBA plus six European VLBI Network (EVN) telescopes—image from a 24 hr observation of O'Sullivan et al. (2011) from 2000 June 5, only 7 weeks earlier in the quasar rest frame. The image in the panel on the right of Figure 5 was generously created for the purpose of this study by Shane O'Sullivan. The Gaussian fitted components' FWHM from Table 3 are represented by circles and ellipses with crosses. These components seem to capture every observed feature, including the north lobe. There is a strong component to the southeast as well as a very weak compact component to the northeast, the putative knot in the northern jet. The locations do not line up perfectly with VSOP, but that might be an artifact of trying to fit features on scales smaller than the synthesized beam. This might also explain the flux density difference in the southeast component (79 ± 15 mJy versus 40 ± 10 mJy). Other contributing factors could be extreme variability and the absolute flux density

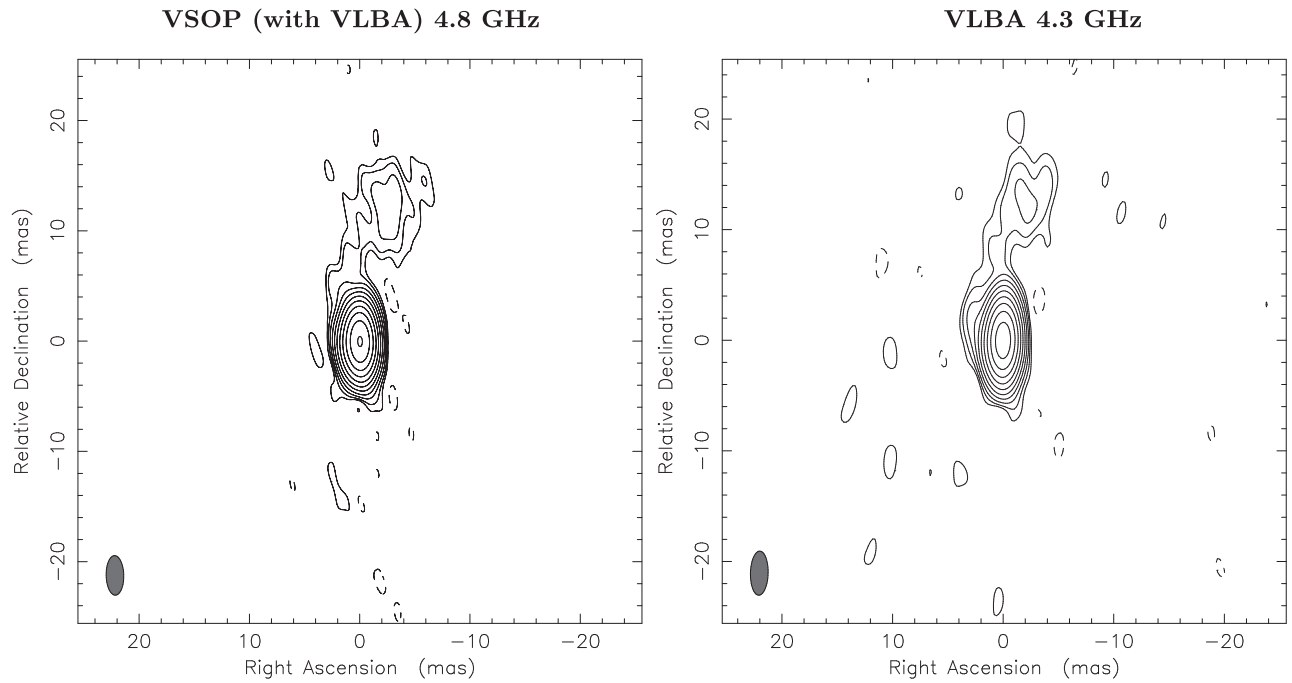

Figure 4. This figure compares the 4.8 GHz VSOP (including the VLBA) observation from 2001 January 23 (left) with the 4.3 GHz VLBA observation from 2014 February 18 (right). The latter observation has far less time on the source; however, the two images separated by 13 yr look remarkably similar. There are no measurable changes to the north lobe within measurement uncertainties as evidenced by Table 3. In the left image, the peak intensity is 641 mJy beam^{-1}, and the lowest level contour is ±0.6 mJy beam^{-1}. The restoring beam is 1.6 mas × 3.59 mas at PA = 1.3°. In the image on the right, the peak intensity is 769 mJy beam^{-1}, and the lowest level contour is ±0.955 mJy beam^{-1}. The restoring beam is 1.59 × 3.99 mas at PA = − 1.5°. The positive contour levels increase by a factor of 2.

calibration of VSOP. In this context, it should be noted that we were unable to retrieve all of the original files used in the VSOP data reduction. Hence, there is some uncertainty in the absolute flux density calibration in the files we could retrieve. There is a possible difference with the calibration of Frey et al. (2002) that indicates ≈40 mJy in the southeast component, we fit 31.2 mJy using the data files that were found. However, it is still consistent within the uncertainties in Table 3. We investigate this component further with higher frequency VLBI in the next subsection.

The primary objective of the *C*-band Gaussian fits in Table 3 is to quantify the apparent motion of the north lobe. Hence, we have included some Astrogeo data that likely have insufficient sensitivity to capture the diffuse lobe flux density accurately. However, they are adequate for finding the position of the north lobe. Based on Table 3 and Figure 4, it seems to have been stationary over a quarter century within uncertainties. Any apparent motion of the northern lobe is masked by the relatively large uncertainties. These uncertainties control the constraints that we can put on an upper bound to the component motion. Figure 6 is a scatter plot of the separation versus time from the Gaussian fits in Table 3. The separation data in Table 3 were fit by least squares with uncertainty in the vertical variable in Figure 6 (Reed 1989). The standard error of the fit is given by the dashed lines. Based on the fit, the lobe advances at 0.006 ± 0.018 mas yr^{-1}, i.e., consistent with no motion. In our chosen cosmology, we have 7.31 pc mas^{-1}, so the apparent velocity of the north lobe relative to the nucleus is $v_{\rm apparent} = (0.13 \pm 0.44)c$. The uncertainties in the data do not allow us to provide much more than an upper bound of $v_{\rm apparent} < 0.57c$.

3.3. High Frequency VLBI

High frequency VLBI observations have the resolution required to define the southeast component. The details of the four high frequency observations are described in Table 4. The first observation is the *X*-band observation performed simultaneously with the first *S*-band entry in Table 1 (Fey & Charlot 2000). The second observation to consider is the global VLBI *X*-band observation that was coincident with the *S*-band observation described in Table 1 and Figure 3. The most curious feature is that the elongated core seen in the global VLBA observation of 2000 June 5 is resolved into a nuclear two component structure. There was an observation at 8.4 GHz with high background noise that we do not include in the table from 2000 June 5 (O'Sullivan et al. 2011).

The two never before published observations from the VLBA archives are presented in Figure 7. First of all, note that the three observations and the 2000 June 5 global VLBI observations at 5 GHz define a consistent axis for the nuclear region at PA ≈ − 165° and based on the *X*-band resolution, it is directed toward the south. This explains the jet geometry. The inner jet is directed at PA ≈ − 165° for about 0.8 mas. At this point it veers abruptly toward the southeast component at PA ≈ 130° (an ≈65° rotation). We postulate that afterward it bends toward the north through the knot in the north jet (3–5 mas out), finally terminating at the north lobe (12.5 mas out). Such behavior up to and through the southeast component is indicative of Doppler abberation and a nearly polar LOS (Lind & Blandford 1985).

Next, we use the high frequency observations to gain clues into the nature of the southeast component . The lack of a detection at 22.4 GHz is unexpected based on the apparent sensitivity of the observations. The 9 hr observation for VLBA project BN0003 during 1996 September 7–8 produced a total of 64 minutes of data on source PKS 1351-018 with 32 MHz bandwidth in a single polarization. The phased VLA (in D-array) was added to the array improving the (still sparse) *u*, *v* coverage and improving the sensitivity. We found an rms noise of ≈1.5 mJy beam^{-1}. Based on the size found at 15 GHz in

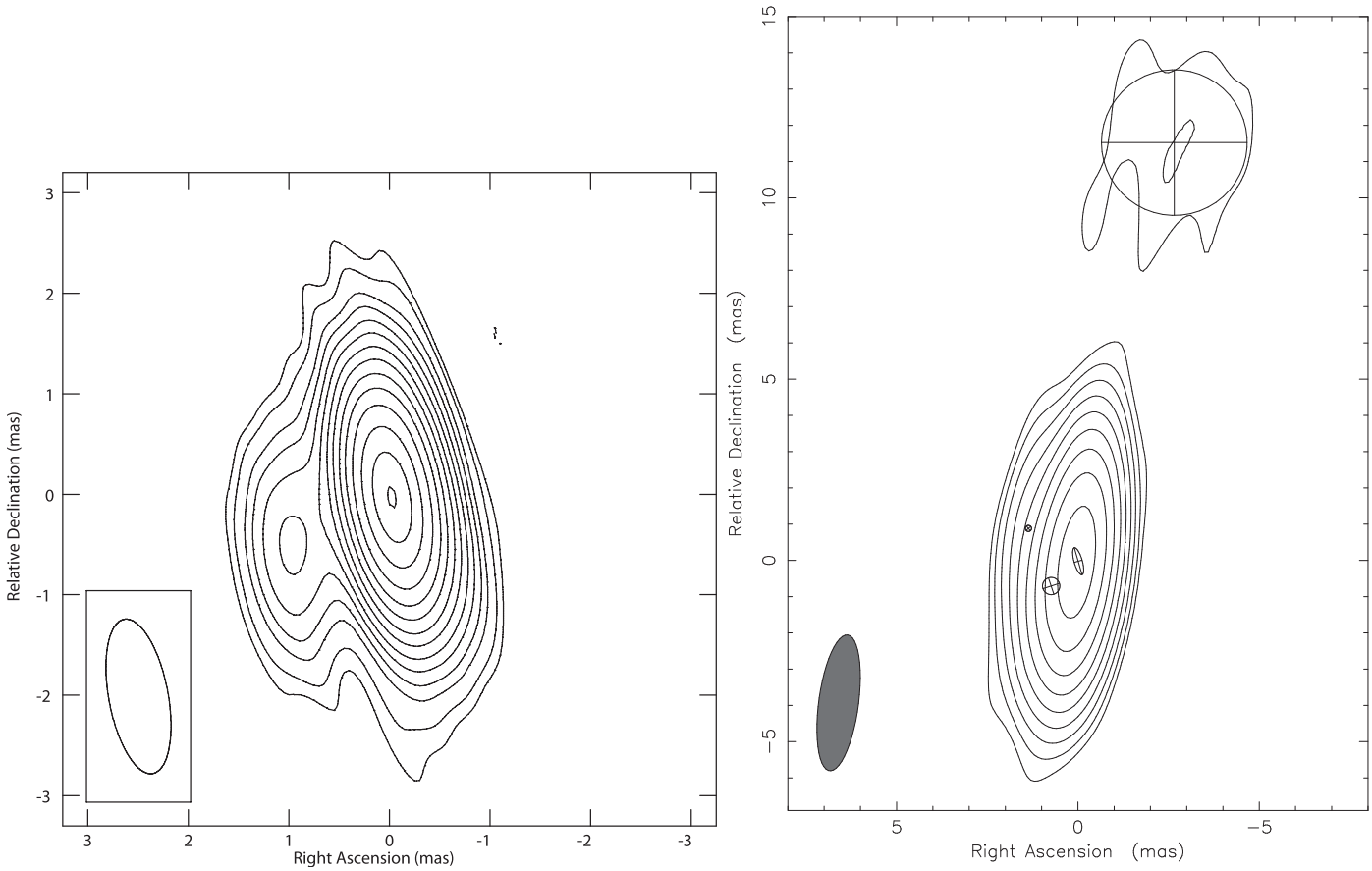

Figure 5. On the left is the 4.8 GHz VSOP image from 2001 January 23, with special weighting to enhance the space–ground baseline data, as reproduced from (Frey et al. 2002). Contours are at −1%, 1%, 1.5%, 2.5%, 3.5%, 5%, 7%, 10%, 14%, 20%, 28%, 40%, 56%, 80%, and 99% of the peak brightness of 547 mJy beam^{-1}. The restoring beam is 0.59 × 1.56 mas at PA = 11°. The image in the panel on the right is a 5 GHz global VLBI image from 2000 June 5. The peak intensity is 663 mJy beam^{-1}, and the lowest level contour is ±1.66 mJy beam^{-1}. The restoring beam is 1.1 × 3.78 mas at PA = − 7.6°. The positive contour levels increase by a factor of 2. The ellipses with crosses are the Gaussian components from Table 3. Note that both observations detect a southeast component.

Table 4, we would have expected to have detected a flux density as low as 7.5 mJy at the 5σ level. Figure 8 shows extrapolated power-law fit from the lower frequency data. We expected 10–15 mJy. There are three possible explanations:

1. There is a flaw in the radio observation introduced by a subtle calibration issue. Although there are no obvious signs of artefacts in the image, the surface brightness of the noise is 2.25 times higher at 22.1 GHz than at 15.4 GHz. We investigated this possibility by imaging 4C 39.25, a very bright source observed during the same observing run. We would expect that such an error would be easier to spot in those data. Nothing was apparent. Further, we imaged the PKS 1351-018 data using various subsets of the antennas, none of which indicated significant emission at the position of the southeast component, or significant changes in the observed morphology.
2. There could be strong synchrotron cooling that makes the spectrum curve downward sharply around 15 GHz.
3. The source might be highly variable. However, consider the following from Table 4. 18.5 days earlier in the quasar rest frame, the southeast component was detected with 22 mJy at 15.4 GHz. 20 days later in the quasar rest frame, it was detected with ≈30 mJy at 8.55 GHz (similar to the estimated flux density in 2002).

We simply do not have enough information to reach a definitive conclusion on the contribution of each of these possibilities. We assume that all of these are factors, the *K*-band image is relatively noisy, and there is a spectral steepening (perhaps not severe). Furthermore, there is some significant (but not extreme) variability. In Figure 8, we look at a scatter plot of the flux density at the four frequency bands in order to try and organize the trend in the difficult to measure quantity. A good measurement requires high resolution, high sensitivity, and high dynamic range. That being said, 15 GHz VLBA is our most reliable data. The only thing stopping a very tight trend in Figure 8 are the two disparate *C*-band flux densities and the 22 GHz non-detection. The 22 GHz data are still a mystery considering the detections of the southeast component within 3

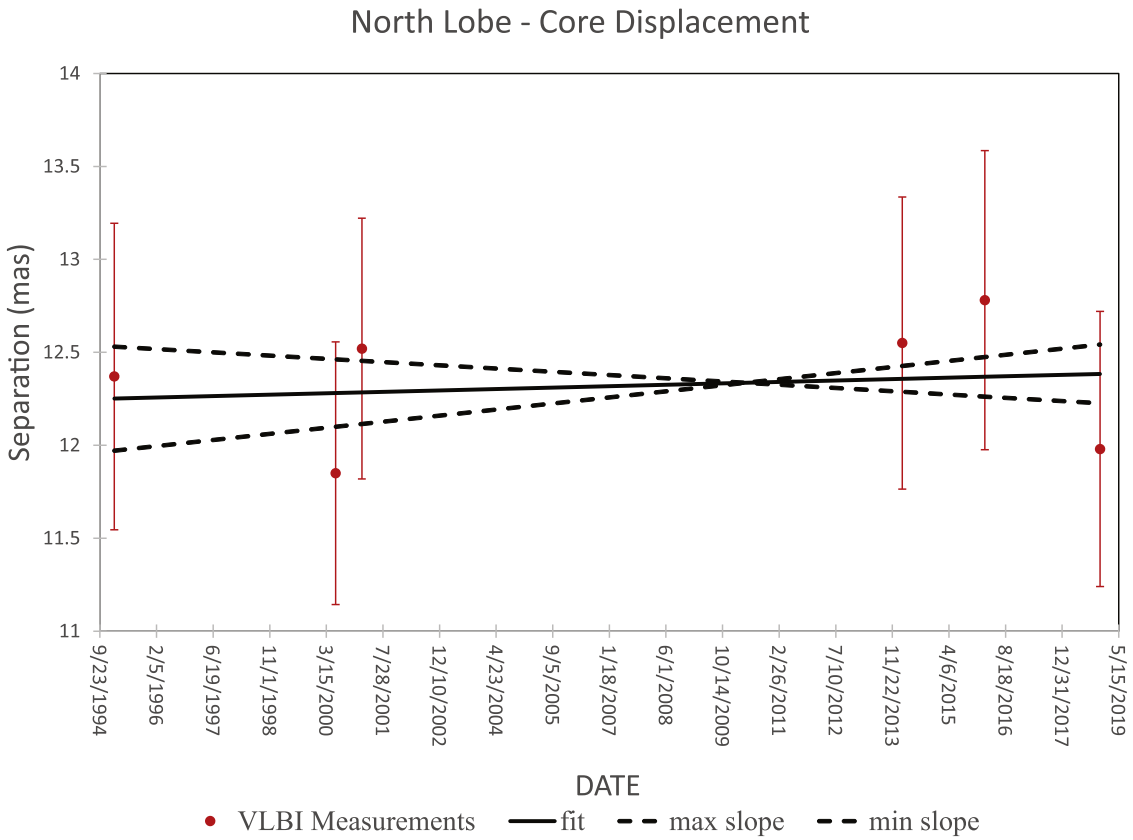

Figure 6. There is formally no motion detected in the northern lobe in our six measurements of its position over 23 yr. Due to the high redshift, the instrumental uncertainties correspond to relatively large physical uncertainties in the true position thereby masking any slow motion. We try to bound the motion with a fit to the data with uncertainty in the vertical variable (Reed 1989). The fit is the solid line and the standard error of the fit is indicated by the dashed lines. The maximum apparent velocity that is compatible with the standard error is $v_{\rm apparent} < 0.57c$.

weeks before and after (in the quasar rest frame). In the following, we will assume that the power-law fit in Figure 8 (spectral index $\alpha \approx 0.98$) applies to the data at frequencies below 15 GHz with some modest (~20%–30%) variability.

4. The Synchrotron SED

This section compiles the radio to millimeter wave data that are used to construct possible physical models of the radio source later in this paper. The results are in Table 5. Since the data have relatively large measurement uncertainty compared to the magnitude of flux density variability of PKS 1351-018, we have averaged the historical data to reduce the uncertainty. Figure 1 is the best example, but we also average at other frequencies when possible. For now, we simply collect the data and create a synchrotron SED that extends from $\nu \sim 6 \times 10^8$ to $\nu \approx 10^{12}$ Hz in the quasar rest frame.

The first column of Table 5 is the observed frequency. This is converted into the logarithm of the frequency in the quasar rest frame in the next column. We then give the flux density with its uncertainty, which is considerable at very low and very high frequencies for individual measurements. We then list the telescope used, the reference to the data, and the comments in the final three columns. We note how many of the frequencies were able to be averaged over at least a modest set of historical observations with the same telescope in the comments column. In our modeling, the low frequency data are very important. The $\nu_{\rm o} = 107$ to $\nu_{\rm o} = 227$ MHz Galactic and Extragalactic All-sky MWA survey (GLEAM) data are very useful, but have much scatter due to the low flux densities (ν designates frequencies in the cosmological rest frame of the quasar and $\nu_{\rm o}$ the observed frequencies; $\nu = (1+z)\nu_{\rm o}$). There were 15 channels and we averaged five at a time in order to get a more robust flux density. Even so, the data do not agree well with the $\nu_{\rm o} = 150$ MHz Tata Institute for Fundamental Research Giant Metrewave Radio Telescope (GMRT) Sky Survey Alternate Data Release (TGSSADR) flux density. The modest low frequency flux density of PKS 1351-018 provides a challenge to survey observations, and TGSSADR has only one data point, so it is more difficult to check its consistency. We also were fortunate to obtain numerous *P*-band observations from JVLA and the one from the VLA. At $\nu_{\rm o} = 340$ GHz, we pick the mean and the standard deviation of 64 observations binned into 15 distinct epochs (each epoch has <10 day spread in the observations in the quasar rest frame) to be the values of the flux density and uncertainty, respectively. These observations span 5.5 yr from 2015–2020. The synchrotron SED is plotted in Figure 9. We added a log-parabolic fit. Unfortunately, the high frequency observations that define the peak are difficult and the uncertainty and scatter are larger than one would like. A carefully calibrated 43 GHz JVLA observation would be very useful. The SED peak is at $\nu_{\rm peak} \approx 5 \times 10^{11}$ Hz. Based on the *blazar sequence* this is at the low end of the peak frequency expected for a flat spectrum Fermi detected quasar with a peak spectral luminosity of $\sim 2 \times 10^{46}$ erg s^{-1} (Ghisellini et al. 2017). Typically, they find $\nu_{\rm peak} \approx 2.0 \times 10^{12}$ Hz for a flat spectrum quasar that is Fermi detected. The integrated luminosity of the SED up to 10^{12} Hz in the quasar rest frame (the limit of our data) is 7×10^{46} erg s^{-1}, or $L_{\rm synch} > 7 \times 10^{46}$ erg s^{-1} since we do not include the high frequency side.

Table 4
Gaussian Fits to High Frequency VLBI Observations

(1) Date	(2) Array/ Frequency	(3) Restoring Beam (mas)	(4) Component	(5) Flux Density (mJy)	(6) r (mas)	(7) Position Angle (°)	(8) FWHM (mas)	(9) Axial Ratio/PA	(10) T_b (K)	(11) Ref.
1997 Jan 11	VLBA	2.2 × 1.0	Core	480 ± 48	0	⋯	0.50	0/24°	⋯	[a]
	8.55 GHz		North lobe	Not detected	Not detected	⋯	⋯	⋯	⋯	⋯
			Southeast component [b]	30 ± 9.3	1.0 ± 0.3	135	0.9	0/30°	⋯	
2002 Jul 24	Global VLBI	1.75 × 0.79	Core	466 ± 46	0	⋯	0.18	1	1.07×10^{12}	[c]
	8.65 GHz		North lobe	11.8 ± 4.7	11.5 ± 0.3	−20.6	2.1	1	2.62×10^{9}	[d]
			Nuclear secondary [b]	233 ± 23	0.65 ± 0.3	−166.6	0.33	1	1.64×10^{11}	
			Southeast component [b]	37.9 ± 8.5	1.2 ± 0.3	141.0	[e]	1	[e]	
1996 Jun 13	VLBA	1.16 × 0.47	Core	529 ± 53	0	⋯	0.75	0.19/ 17.6°	1.99×10^{11}	[d]
	15.4 GHz		North lobe	Not detected	Not detected	⋯	⋯	⋯	⋯	
			Southeast component	17.4 ± 4.6	1.2 ± 0.2	145.0	0.0	⋯	⋯	
1996 Sep 7	VLBA	1.16 × 0.47	Core	398 ± 40	0	⋯	0.76	0.22/ 18.7°	3.61×10^{10}	[d]
	22.1 GHz		North lobe	Not detected	Not detected	⋯	⋯	⋯	⋯	⋯
			Southeast component	<7.5		⋯	⋯	⋯	⋯	⋯

Notes.
[a] Fey & Charlot (2000). Flux density error estimate of southeast component uses the 26% uncertainty computed in the 2002 observation added in quadrature with roundoff error.
[b] Sparse (u, v) coverage at baselines long enough to model the ∼1 mas nucleus.
[c] Pushkarev & Kovalev (2012).
[d] This paper.
[e] Effectively a point source, T_b estimate ill-defined.

5. Electromagnetic Signature of the Accretion Flow

In this section, we explore the optical spectrum, near-IR, and mid-IR photometry, in order to define the thermal emission of the accretion flow from the rest-frame UV to the near-IR (the signature of the quasar). There are two optical spectra of this quasar. The first observation was in 1985 with the Anglo-Australian Telescope (AAT; Dunlop et al. 1989). There is a 2003 March 23 Sloan Digital Sky Survey (SDSS) spectrum that we show in the top panel of Figure 10. It has been corrected for Galactic extinction using the extinction values in the NASA Extragalactic Database (NED) applied to the models of Cardelli et al. (1989). There is very deep Lyα absorption from intervening gas short-ward of the Lyα emission from PKS 1351-018. The blue side of the Lyα broad emission line is completely truncated. The continuum spectral index defined in terms of the flux density as $F_\nu \propto \nu^{-\alpha_\nu}$ is $\alpha_\nu \approx 0.78$ long-ward of Lyα. This is typical of a radio-quiet quasar. The Hubble Space Telescope (HST) composite spectral index was found to be $\alpha_\nu \approx 0.86$ (Zheng et al. 1997). Thus, this has a very strong accretion signature with very little influence of the jet synchrotron emission long-ward of Lyα (see IR discussion below). This means that there is no significant synchrotron dilution from the jet. Looking at the peak and turnover at $\approx 10^{12}$ Hz in the synchrotron SED in Figure 10 and the SDSS SED in the bottom panel of Figure 10 this seems clear. The bottom panel of Figure 10 compares the SDSS data to the HST composite shape from Laor et al. (1997) and Zheng et al. (1997) to the spectrum in the top panel after rescaling to the continuum level of PKS 1351-018. We added photometry points from archival mid-IR data in NED and IR observation found in the Data Release 11 of the United Kingdom Infrared Telescope (UKIRT) Deep Sky Survey[19] (Lawrence et al. 2007). This shows the characteristic 1 μm dip in the quasar spectrum that appears in the composite. Thus, there is no evidence of synchrotron dilution even on the upslope from the dip. Note the three photometry points from Dunlop et al. (1989). The B-band and R-band photometry lie right on top of the SDSS spectrum indicating very little variability between 1985 and 2003. The K-band data point in Dunlop et al. (1989) was taken with UKIRT, but disagrees with the value from the UKIRT Deep Sky Survey.

We can use the spectrum in Figure 10 to estimate the bolometric thermal luminosity from the accretion flow, $L_{\rm bol}$. The desired estimate does not include reprocessed radiation in the infrared from molecular clouds that are far from the active nucleus (not shown in the bottom panel of Figure 10). This would be double counting the thermal accretion emission that is reprocessed at midlatitudes (Davis & Laor 2011). The most direct method is to use the UV continuum as a surrogate for $L_{\rm bol}$. From the spectrum in Figure 10 and the formula expressed in terms of quasar cosmological rest-frame wavelength, λ_e, and spectral luminosity, L_{λ_e}, from Punsly et al. (2016),

$$L_{\rm bol} \approx (4.0 \pm 0.7)\lambda_e L_{\lambda_e}(\lambda_e = 1350\ \text{Å}) \approx (1.45 \pm 0.25) \times 10^{47}\ \text{erg s}^{-1}. \quad (8)$$

The bolometric correction was estimated from a comparison to HST composite spectra of quasars with $L_{\rm bol} \approx 10^{46}$ erg s^{-1} (Laor et al. 1997; Zheng et al. 1997; Telfer et al. 2002).

[19] http://wsa.roe.ac.uk/index.html

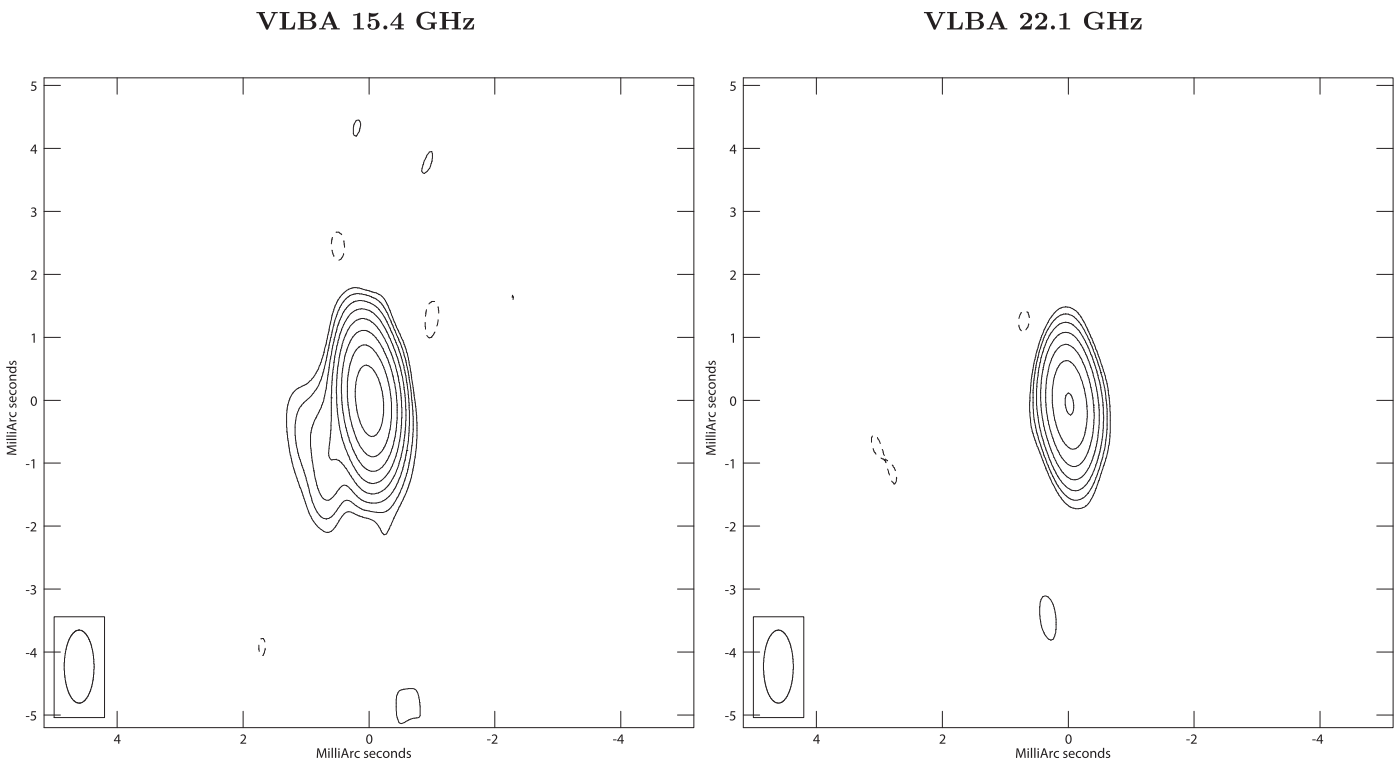

Figure 7. In the panel on the left is the 15.4 GHz VLBA image from project BK0042 on 1996 June 13. In the panel on the right is the 22.1 GHz VLBA image from 1996 September 7. To aid comparison, both images are created with the same restoring beam, the naturally weighted beam from the 15.4 GHz observation, 1.16×0.47 mas at PA $= 1.9°$. The bottom contour is ± 3 times the rms noise 1.95 mJy beam^{-1} (4.47 mJy beam^{-1}) and the peak intensity is 405 mJy beam^{-1} (298 mJy beam^{-1}) at 15.4 (22.1) GHz. The positive contours increase by factors of 2. Even though the two observations occurred only 18.5 days apart in the quasar rest frame, the prominent southeast component seen in the left panel is absent in the right panel.

Since Lyα is truncated by the Lyα forest, the only strong broad emission line (BEL) in the SDSS spectrum is C IV. In Figure 11, we fit the C IV emission line into a common decomposition format, two broad lines and one narrow line (Brotherton 1996; Sulentic et al. 2000; Marziani et al. 2010). The blue (red) broad Gaussian component has a line center shifted $\approx$3900 km s^{-1} (≈ -390 km s^{-1}) with an FWHM of $\approx$3560 km s^{-1} ($\approx$4860 km s^{-1}) and a luminosity of $\approx 9.3 \times 10^{43}$ erg s^{-1} ($\approx 1.7 \times 10^{44}$ erg s^{-1}). The narrow line profile has a FWHM $\approx$1660 km s^{-1} and a luminosity of $\approx 9.3 \times 10^{43}$ erg s^{-1}. There are two odd things about this line. First, it is a relatively weak broad line. The rest-frame equivalent width (EW) is $\approx$13 Å and if we include the narrow line this only increases to EW $\approx$ 17 Å. While the typical value from the HST sample of Telfer et al. (2002) is $\sim$60 Å. As discussed earlier this is not a consequence of synchrotron dilution. We note that such small EWs are not unheard of as documented in Baldwin et al. (1989) and Diamond-Stanic et al. (2009). The other odd feature is the strong blue excess, which is typical of high luminosity radio-quiet quasars, while quasars with powerful radio jets and lobes tend to have a red excess (Richards et al. 2002; Punsly 2010). The blueshifted Gaussian component is often considered evidence of a wind driven by the radiation pressure from the accretion flow (Brotherton et al. 1994; Murray et al. 1995; Brotherton 1996; Netzer & Marziani 2010; Sulentic et al. 2017). This behavior seems to be explained by the large $L_{\rm bol}$ found in Equation (8). The quasar might have a high Eddington luminosity, but we have no reliable virial estimate in the absence of a broad low ionization line to measure.

6. γ-Ray Behavior

The 10 yr (from 2008–2018) average γ-ray luminosity detected by Fermi-LAT from 0.1–500 GeV (observed energy) is $L_\gamma = 5.78 \times 10^{47}$ erg s^{-1} (Sahakyan et al. 2020). The temporal behavior of the γ-ray emission has been studied with low time resolution due to the low number statistics (Li et al. 2018). In this section, we explore higher time resolution in order to ascertain the peak γ-ray luminosity. The data reduction method is defined in Li et al. (2018). In summary, the publicly available Fermi-LAT Pass 8 data (P8R3_SOURCE_V2) and Fermitools were used to perform the data analysis. The data from 2008 August 4 to 2018 August 4 with the energy range from 100 MeV to 100 GeV was selected. We removed the γ-ray events with zenith angle greater than 90° and the quality-filter cuts (DATA_QUAL==1 && LAT_CONFIG==1) are applied. We selected photons set within a 10° region of interest and performed a unbinned likelihood analysis. The script `make4FGLxml.py`[20] was used to generate the background model, which include all 4FGL-DR2[21] sources within 15° around the target as well as `gll_iem_v07.fits` and `iso_P8R3_SOURCE_V2_v1.txt`. The spectra of the point sources within 10° around the center and the normalizations of the two diffuse emission backgrounds were set free. We determine the significance of the flare with the test statistic (TS; Mattox et al. 1996). The TS is defined as TS $= 2 \ln L/L_0$, where L and L_0 are the maximum likelihood values for the model with and without target source, respectively. The

[20] https://fermi.gsfc.nasa.gov/ssc/data/analysis/user/make4FGLxml.py
[21] https://fermi.gsfc.nasa.gov/ssc/data/access/lat/10yr_catalog/

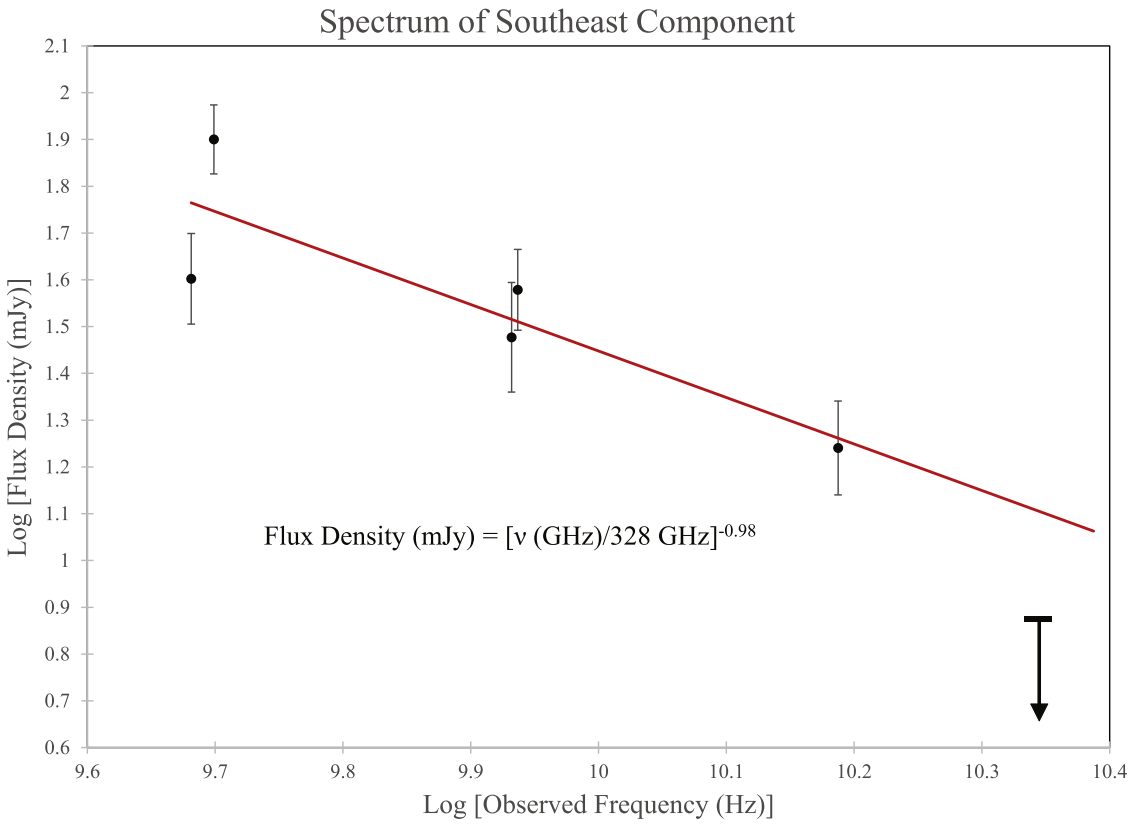

Figure 8. Based on all the available observations, this is our chosen characterization of the spectrum of the southeast component. It is a component only 1 mas from the core and only ∼3%–5% as bright. It is apparently variable as well, but this magnitude is difficult to determine as a result of the uncertainty of fitting a relatively faint component so close to a bright core. Variations on the order ±30% seem consistent with the scatter to the fit of the data from 4.8–15.4 GHz. The spectral fit is therefore, an average fit and it is clearly steep. We use the spectral index of $\alpha = 0.98$ in our theoretical models of the source. Our estimates of jet power do not rely strongly on this quantity. We also note that there might be a spectral turnover at ≈15 GHz.

quantity TS was identified with a statistical significance of $\sqrt{\mathrm{TS}} = n\sigma$ in Equation (22) and Figure 3 of Mattox et al. (1996). We consider two likely flares in 2011 and 2016 that were previously identified with ∼5 month time sampling (Li et al. 2018). Since we already know that the flare is present, Figure 12 considers higher time resolution of the Fermi-LAT light curves at these epochs. We consider 3 week bins or 4.5 days in the quasar rest frame.

The vertical axis in Figure 12 is the 0.1–100 GeV luminosity. The first flare seems more prolonged, but the second flare was brighter. The peak flare luminosity was $\approx 6 \times 10^{48}$ erg s^{-1}. With finer sampling (3 days), this increases to $\approx 10^{49}$ erg s^{-1}, but TS falls below 25, TS $\gtrsim$ 20. The SED in the γ-ray region is very steeply decreasing power law ($\alpha \approx 2$) as expected for strong external inverse Compton cooling from the existence of the luminous quasar environment that was described in the last section (Marcotulli et al. 2020; Sahakyan et al. 2020). This combined with the high redshift indicates that most of the γ-ray luminosity is most likely at observed energies <0.1 GeV. Thus, it is quite possible that the 2016 γ-ray flare is of comparable luminosity to some of the strongest known γ-ray flares (Abdo et al. 2011).

7. Synchrotron Self-absorbed (SSA) Power-law Fit to the Radio Data

A synchrotron SSA power law for the observed flux density, S_{ν_ϕ}, is the solution to the radiative transfer in a homogeneous medium such as a uniform spherical volume (Ginzburg & Syrovatskii 1965; van der Laan 1966):

$$S_{\nu_\phi} = \frac{S_o \nu_o^{-\alpha}}{\tau(\nu_o)} \times (1 - e^{-\tau(\nu_o)}),$$
$$\tau(\nu_o) = \overline{\tau} \nu_o^{(-2.5+\alpha)}, \quad (9)$$

where $\tau(\nu)$ is the SSA opacity, S_o is a normalization factor, and $\overline{\tau}$ is a constant. The wide spectral peak requires three SSA power-law components. Adding a fourth SSA power law does not improve the fit. In Figure 13, we show the three components of the SSA power-law fit that are naturally associated with the unresolved nucleus, the southeast component and the north lobe. The power laws for the core, southeast component, and north lobe are approximated by the data from $\nu_o = 5$ to $\nu_o = 22$ GHz in Table 5, Figure 8, and the VLBI data in Tables 1, 3 and 4, respectively. Fine adjustment of the SSA power-law parameters proceeds until the residuals (see Equation (3)) of the fit to the total flux density from $\nu_o = 120$ MHz to $\nu_o = 22$ GHz are minimized. The fit is based on two important assumptions that are motivated by the observations in Tables 1, 3, and 4 that are described below.

7.1. Assumption 1: VLBI Does Not Capture All of the North Lobe Flux at High Frequency

Since the north lobe is a diffuse, steep spectrum, component, there will be a tendency for VLBI to resolve out some of the

Table 5
Radio Data for PKS 1351-018

ν_o Observed Frequency (MHz)	log ν Quasar Rest Frame (Hz)	Flux Density (mJy)	Telescope	Reference	Comments
123^{+20}_{-16}	8.76 ± 0.06	214.5 ± 27.8[a]	MWA[b]	Wayth et al. (2015) [c]	5 bin average
150	8.76	185.0 ± 27.8[a]	GMRT	Intema et al. (2017), Hurley-Walker (2017)	TGSSADR
165 ± 15	8.89 ± 0.04	246.4 ± 37.0[a]	MWA[b]	Wayth et al. (2015) [c]	5 bin average
208 ± 19	8.99 ± 0.04	276.8 ± 41.5[a]	MWA[b]	Wayth et al. (2015) [c]	5 bin average
330	9.19	329.7 ± 33	VLA	This paper	A-array
340	9.20	362 ± 50	VLA/VLITE	This paper, Clarke et al. (2016), Polisensky et al. (2016) [d]	15 epoch average
365	9.24	371 ± 37	Texas Interferometer	Douglas et al. (1996)	
960	9.66	510 ± 51	RATAN-600	Kovalev et al. (1999)	
1400	9.82	733 ± 37	VLA D-array	Condon et al. (1998)	NVSS
1400	9.82	709 ± 35	VLA B-array	Becker et al. (1995)	FIRST
1484	9.84	743 ± 37	VLA A-array	Neff & Hutchings (1990)	
2100	10.00	850 ± 85	ATCA	Calibrator database[e]	
2700	10.10	897 ± 53	ATCA	Calibrator database[e]	8 epoch average
4900	10.36	905 ± 42	VLA and ATCA	Average of Figure 1	
8470	10.60	812 ± 70	VLA	NVAS, this paper	27 epoch average
14,900	10.85	669 ± 39	ATCA	Calibrator database[e]	8 epoch average
22,400	11.02	542 ± 35	ATCA	Calibrator database[e]	8 epoch average
33,000	11.19	373 ± 56	ATCA	Calibrator database[e]	
43,000	11.31	400 ± 80	VLA	Calibrator list[f]	
43,000	11.31	303 ± 61	ATCA	Calibrator database[e]	
43,000	11.31	373 ± 56	ATCA	Calibrator database[e]	
90,000	11.63	177 ± 18	IRAM 30 m	Steppe et al. (1995)	
93,000	11.64	170 ± 50	ATCA	Calibrator database[e]	
230,000	12.03	65 ± 13	IRAM 30 m	Steppe et al. (1995)	

Notes.
[a] Uncertainty from Hurley-Walker (2017).
[b] Murchison Widefield Array.
[c] GLEAM:https://vizier.u-strasbg.fr/viz-bin/VizieR-3?-source=VIII/100/gleamegc.
[d] VLA Low Band Ionospheric and Transient Experiment (VLITE). Data provided by Wendy Peters.
[e] https://www.narrabri.atnf.csiro.au/calibrators.
[f] https://science.nrao.edu/facilities/vla/observing/callist.

diffuse emission due to limited dynamic range associated with imperfect (u, v) coverage. This effect is most pronounced at high frequency due to the lower flux density. This is clearly evident in the deep VLBA image at 15.4 GHz in Table 4 that does not detect the north lobe, even though we expected at least 6.5 mJy to be present. Other evidence of this is the 2000 June 5 *C*-band observation in Table 3. This is the longest VLBI (which includes the VLBA baselines) observation (best (u, v) coverage) and it detects the largest flux density of the north lobe of any *C*-band observation. To compensate for this effect, the fit to the north lobe flux is biased toward the top of the error bars at high frequency. This is a valid compensatory device if the observations are sufficiently sensitive (i.e., large fractions of the flux are not resolved out). Thus, the three long duration *C*-band VLBI observations before 2014 in Table 3 are used in the fit to Figure 13 and the observations with short scans and poor (u, v) coverage from 2014 onward are ignored. A direct fit to the data without this biasing toward the top of the error bars yields a power law with $\alpha = 0.85$. We consider the bias toward the tops of the high frequency error bars in Figure 13, which yields $\alpha = 0.75$, to be a more plausible reconstruction of the physical source of lobe emission that is consistent with the observed data.

7.2. Assumption 2: The Knot in the North Jet is Negligible to the Fit

The knot in the north jet that appears in Table 3 is not considered as an important contributor to the total flux density at any frequency for the following reasons.

1. The knot in the north jet is only detected at the *C* band. Thus, there is no spectral data and therefore no basis to extrapolate this to other frequencies.
2. According to Table 3, the feature is not detected at the *C* band in 1995 January 28 and only has 4 mJy in the full track VLBA observation in 2001 January 23.
3. The feature seems to move from 1.6 to ~5.5 mas when it is detected in Table 3 and might not be the same feature.
4. At the *C* band, it is much weaker than the nucleus and does not affect the fit in this region. The fit to the total flux density is determined by the core spectrum at all frequencies above the *C* band.
5. The knot in the north jet is at least one order of magnitude smaller than the north lobe in Table 3. Being so compact, it is likely that the low frequency spectral turnover is at much higher frequency than the north lobe (van der Laan 1966; Moffet 1975; Ezeugo & Ubachukwu 2010). Thus, the knot likely contributes insignificantly at

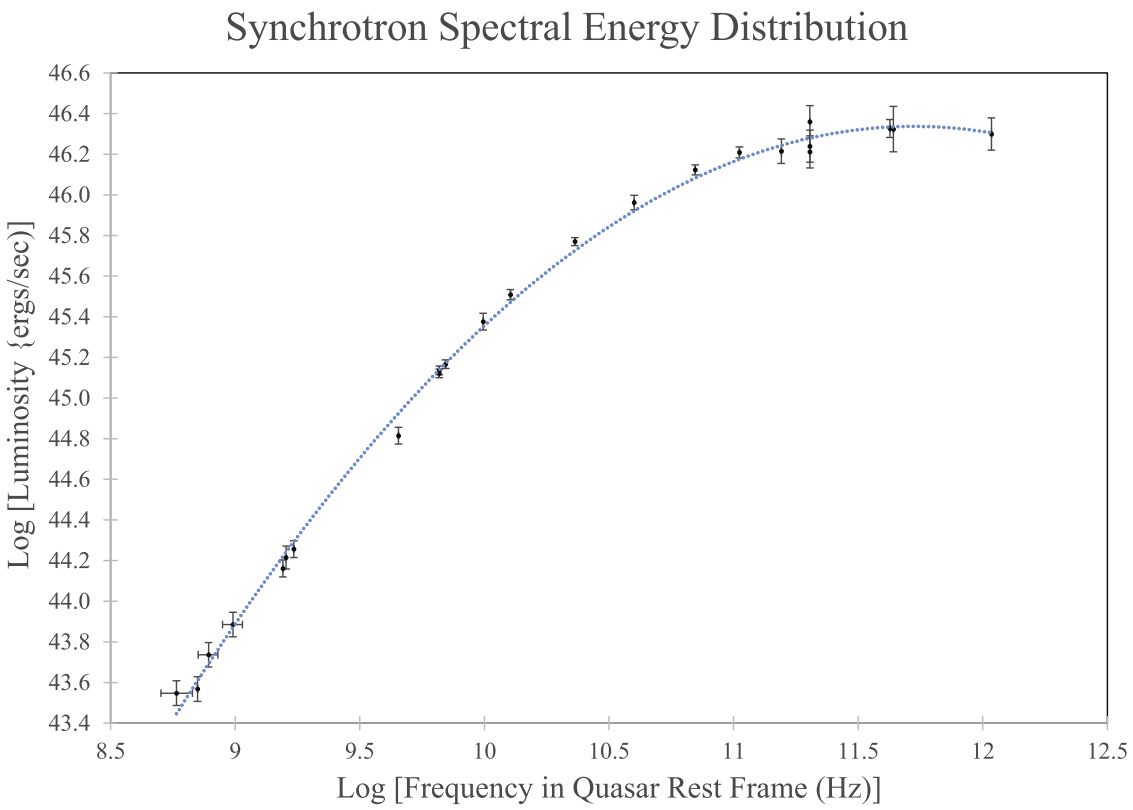

Figure 9. The synchrotron SED created from the data in Table 5. The luminosity of the low frequency portion of the SED (the plotted portion) has a luminosity of $\gtrsim 7 \times 10^{46}$ erg s^{-1}. The full synchrotron luminosity most certainly exceeds 10^{47} erg s^{-1}. The peak of the SED is $\nu_{\rm peak} \approx 5 \times 10^{11}$ Hz in the quasar rest frame.

frequencies below 350 MHz compared to the north lobe (where the north lobe is prominent).

6. As noted above, a fourth SSA power law does not improve the fit to the total flux density.

8. A Physical Model of the North Lobe SSA Power Law

Once an SSA power law is chosen for the north lobe, we are interested in a physical model that is responsible. Complicated dynamics are most likely occurring in the radio lobe (Blundell & Rawlings 2000). In general, there are fine-scale features such as shock fronts and filaments embedded within the diffuse lobe plasma. However, our image in Figure 3 is a structure-less plume that we fit as a circular Gaussian. There is no observational evidence to justify a model more complicated than a homogeneous, spherical, single zone of plasma. Single zone spherical models are a standard technique even in blazar jet calculations out of practical necessity, including previous treatments of this source (Ghisellini et al. 2010; Marcotulli et al. 2020; Sahakyan et al. 2020). A simple homogeneous spherical volume model or plasmoid has historically provided an understanding of the spectra and the time evolution of astrophysical radio sources (van der Laan 1966). We have used this formalism to study a panoply of phenomena, major flares in a Galactic black hole, a γ-ray burst, and flares in a radio-quiet quasar (Reynolds et al. 2009, 2020; Punsly 2012, 2019). Most importantly, we used this method in Punsly et al. (2020) to study the radio lobes in the super-luminous radio quasar, 3C 82 (which should be consulted for the details of the calculational method). The SSA turnover provides information on the size of the region that produces the preponderance of emission. This can be tied directly to the image in Figure 3. Furthermore, these models do not need to invoke equipartition in order to produce a solution.

We have established three physical constraints. First, the FWHM of the north lobe of the 2002 *S*-band observation (the best depiction of the lobe) in Table 1 constrains the sphere radius, R,

$$R \approx 3.3 \text{ mas}. \tag{10}$$

Second, the apparent velocity, $v_{\rm app}$, is bounded by 23 yr of *C*-band radio images as indicated in Figure 6,

$$v_{\rm app} < 0.57c. \tag{11}$$

Third, the light-curve variability analysis of the flare in Figure 2 and Equation (6) provide an approximate constraint on the LOS to the jet axis, θ,

$$\theta < \theta_{\rm max} \sim 10^{\circ}. \tag{12}$$

Note that this constraint is looser than Equation (6) because that derivation assumed no uncertainty arising from the fitting technique in Figure 2. Equations (11) and (12) combine to give a constraint on δ. From Rees (1966) and Ginzburg & Syrovatskii (1969),

$$\beta_{\rm app} \equiv \frac{v_{\rm app}}{c} = \frac{\beta \sin\theta}{1 - \beta\cos\theta}, \tag{13}$$

where β is the three-velocity of the moving plasmoid. Combining the definition of the Doppler factor, $\delta = \sqrt{1-\beta^2}/(1-\beta\cos\theta)$, with Equations (11) and (12) yields an equivalence to a constraint on the Doppler factor in our models. This can be emphasized by writing the Doppler factor as $\delta(\beta_{\rm app}, \theta)$.

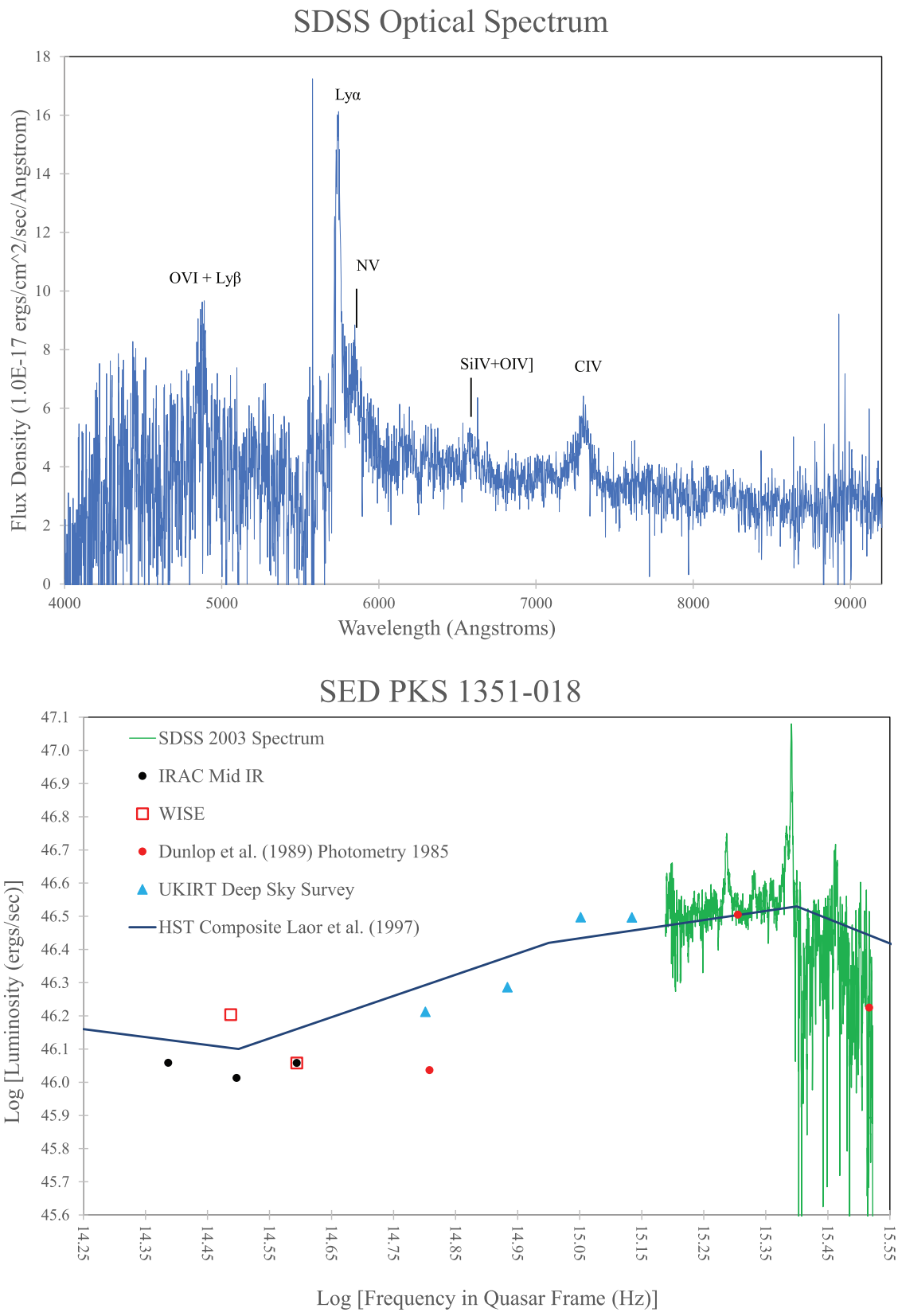

Figure 10. The top panel is the SDSS optical spectrum. There is strong Lyα absorption short-ward of the Lyα BEL. The prominent BELs are indicated. The bottom panel is the SED that includes some photometry points at different epochs. This is compared to the composite HST based spectrum (Laor et al. 1997; Telfer et al. 2002). The rest-frame near-IR to far-UV SED is typical of a radio-quiet spectrum. Optical and IR photometry at other epochs indicate very low variability compared to a blazar. This is consistent with the apparent turnover of the synchrotron SED at $\nu_{\rm peak} \approx 5 \times 10^{11}$ Hz indicated in Figure 9.

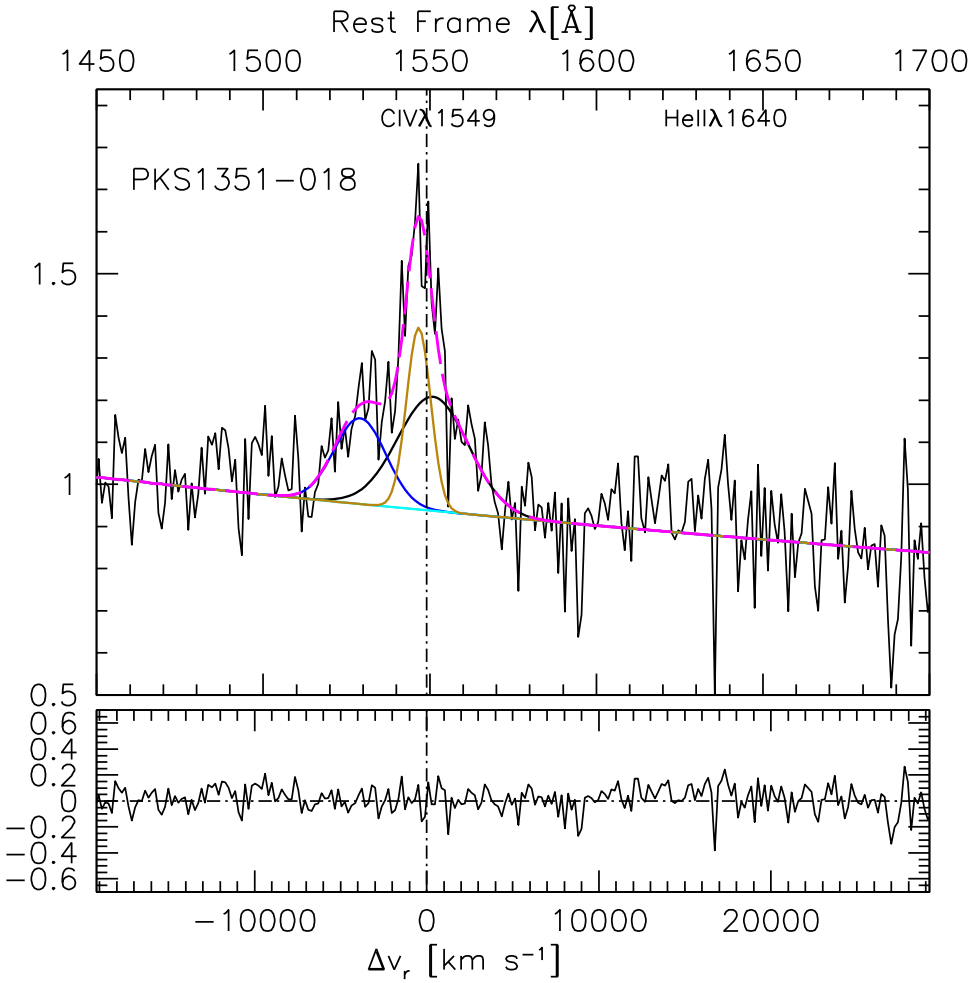

Figure 11. Even though the SDSS spectrum is noisy, it is of sufficient signal to noise to reveal the nature of the C IV emission line. The vertical axis is the flux density in the rest frame of the quasar in units of 3.7×10^{-15} erg s^{-1} cm^{-2} Å^{-1}, the continuum level at 1450 Å. The yellow Gaussian component is the narrow line emission. There are two broad components that were fit. The broader, more luminous of the two is slightly redshifted and is plotted in black. There is a highly blueshifted Gaussian component plotted in blue. This is evidence of a strong, outwardly driven high ionization wind.

The value of minimum lepton energy, $E_{\rm min}$, is not constrained directly by observation. Values of $E_{\rm min} = m_e c^2$ and $E_{\rm min} = 2.6 m_e c^2$ are used in Marcotulli et al. (2020) and Sahakyan et al. (2020), respectively, to fit the synchrotron peak and the inverse Compton spectrum from the nucleus. Here, m_e denotes the electron mass. Since this is the region with the most energetic electrons, we do not expect $E_{\rm min}$ to be larger in the less energetic north lobe. We also note that Celotti & Ghisellini (2008) have argued that $E_{\rm min} = m_e c^2$ based on fits to blazar jet spectra in the soft X-ray band. Thus, we initially consider $E_{\rm min} = m_e c^2$ and explore slightly higher values later. There is not a unique solution to the physical parameters of the north lobe that recreate the fit in Figure 13. In this section we explore the solution space as calculated in Punsly et al. (2020).

8.1. Kinematics of the Lobe Solution

We separate the energy content of the turbulent magnetized lobe into two pieces. The first is the kinetic energy of the protons, $\mathcal{K}$(protonic),

$$\mathcal{K}(\text{protonic}) = (\gamma - 1) M c^2, \tag{14}$$

where M is the mass of the plasmoid and γ is the Lorentz factor in the quasar rest frame. The other component is the lepto-magnetic energy, E(lm), the volume integral of the leptonic internal energy density, U_e, and the magnetic field energy density, U_B. In a spherical volume,

$$E(\text{lm}) = \int (U_B + U_e)\, dV = \frac{4}{3}\pi R^3 \times \left[\frac{B^2}{8\pi} + \int_{\Gamma_{\rm min}}^{\Gamma_{\rm max}} (m_e c^2)(N_\Gamma E^{-n+1}) dE \right], \tag{15}$$

where in the proper frame, B is the magnetic field, N_Γ is the normalization of the number density power law, and $\Gamma(m_e c^2)$ is the lepton energy. The corresponding energy density is $U(\text{lm}) \equiv U_e + U_B$. The leptons also have a kinetic energy analogous to Equation (14),

$$\mathcal{K}(\text{leptonic}) = (\gamma - 1) \mathcal{N}_e m_e c^2, \tag{16}$$

where $\mathcal{N}_e$ is the total number of leptons in the lobe.

There are protonic and leptonic energy fluxes due to bulk motion. The protonic energy flux is approximately the kinetic energy flux,

$$\mathcal{E}(\text{proton}) = N(\gamma - 1)\gamma v_{\rm adv} m_p c^2, \tag{17}$$

where m_p is the mass of the proton, N is the proper number density, and $v_{\rm adv}$ is the advance speed of the lobe in the quasar

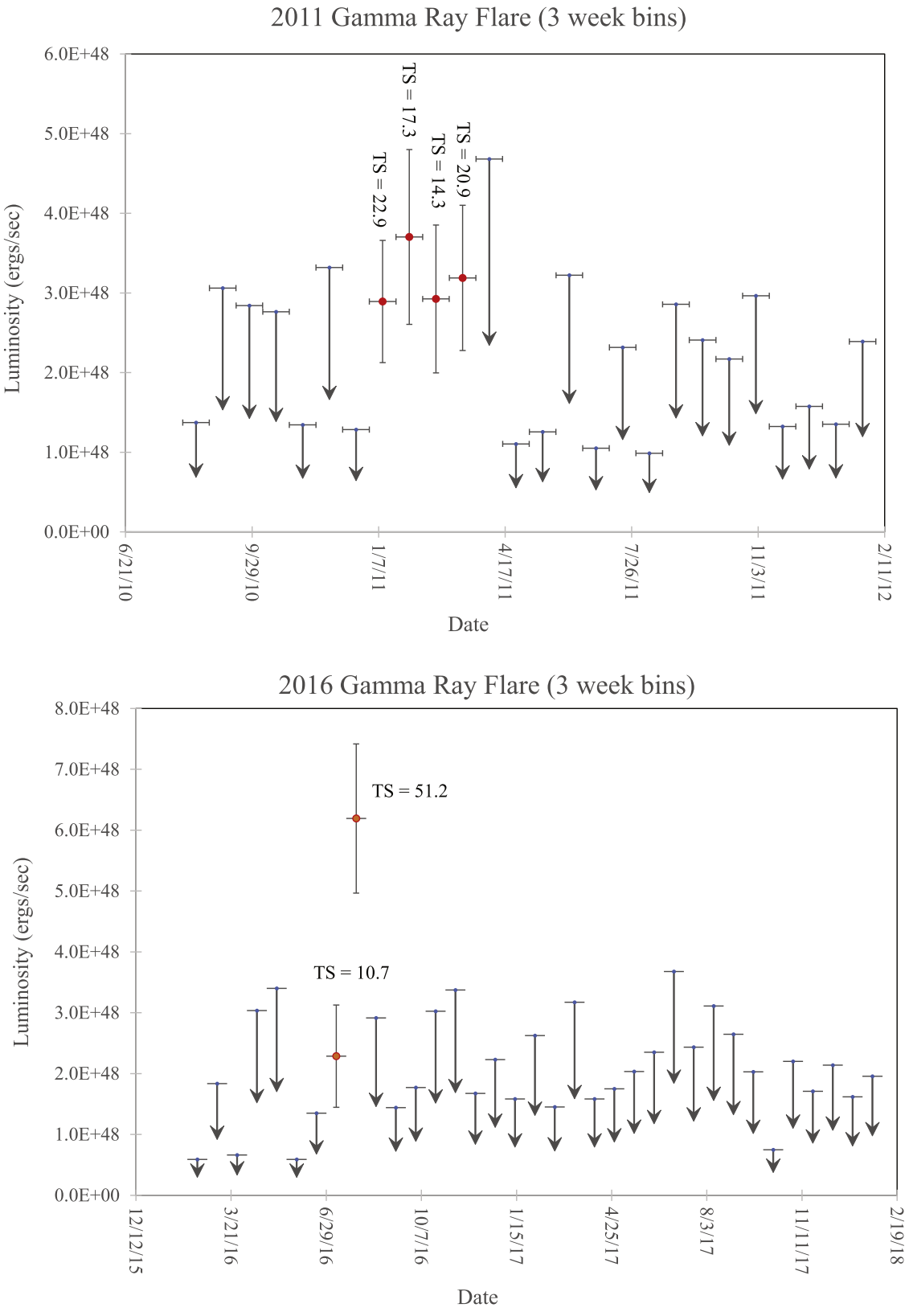

Figure 12. The top panel is the light curve of the 2011 flare sampled in 3 week bins. It is detected in a few consecutive bins but with TS < 25. This suggests a prolonged faint flare. The vertical axis is the 0.1–100 GeV luminosity. The 2016 flare is plotted similarly in the bottom panel.

rest frame. The magneto-leptonic energy flux is

$$\mathcal{K}(\text{magneto} - \text{leptonic}) = N\gamma v_{\text{adv}}[\gamma\mu c^2], \tag{18}$$

where μ is the specific enthalpy (Punsly 2008). The specific enthalpy decomposes as

$$N\mu = U(\text{lm}) + P, \tag{19}$$

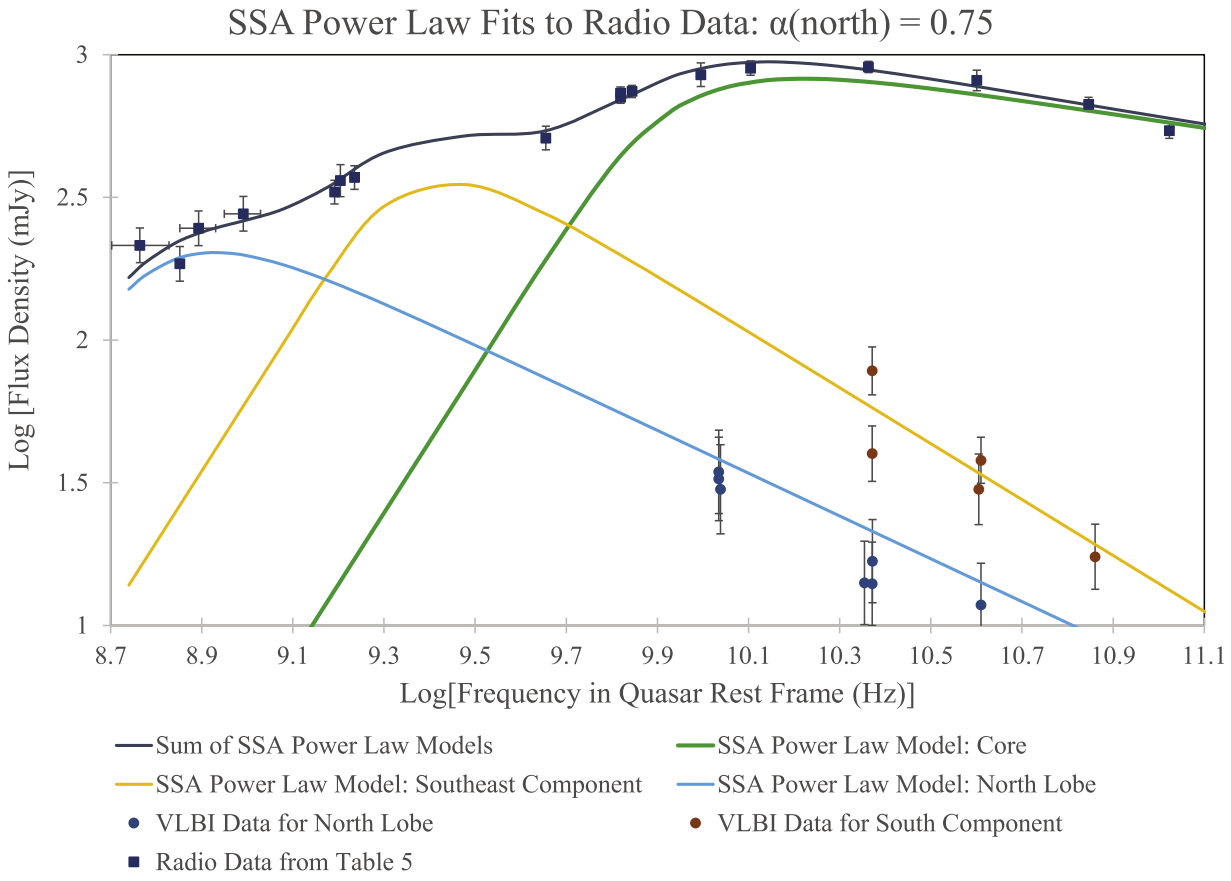

Figure 13. The figure shows the best fit of the three component SSA power-law model to the total flux density of PKS 1351-018. A realistic fit to the north lobe should be biased toward the top of the high frequency error bars for this diffuse structure due to the limited dynamic range of these VLBI data.

where the relativistic pressure, $P \approx (1/3)U(\mathrm{lm})$ (Willott et al. 1999).

With the leptonic assumption, Equation (18) implies that the kinetic luminosity (jet power), Q_{lm}, is

$$Q_{\mathrm{lm}} = \int [\mathcal{K}(\mathrm{magneto} - \mathrm{leptonic})] dA_{\perp} + L_{\mathrm{r}}, \qquad (20)$$

where $dA_{\perp}$ is the cross-sectional area element normal to the jet axis and L_{r} is the energy flux lost to radiation.

The first thing that we noticed about the infinite set of solutions that conform to Equations (10)–(12) is that most of this domain yields solutions that are extremely inertially dominated, $U_e \gg U_B$. The results are plotted in Figure 14 for the four corners of the rectangular domain of the two-dimensional set of preassigned values of $3.0\,\mathrm{mas} < R < 3.5\,\mathrm{mas}$ and $5^{\circ} < \theta < 10^{\circ}$. There is no solution near equipartition with the constraint of Equation (11) imposed, $\beta_{\mathrm{app}} < 0.57$.

These extremely inertially dominated solutions are disfavored on both theoretical and empirical grounds. Theoretically, the pair plasma is highly energetic with large random velocities, and one would expect a relatively strong tangled magnetic field to form. Empirically, the radio lobes of powerful Fanaroff–Riley II (FR II) radio galaxies have magnetic fields that tend to be near equipartition or slightly below this (Fanaroff & Riley 1974; Kataoka & Stawarz 2005; Ineson et al. 2017). A large sample of FR II radio galaxy lobes was studied in X-rays and with multifrequency radio imaging (Ineson et al. 2017). The X-ray observations were used to determine the inverse Compton emission (primarily of the cosmic microwave background) and the radio images were used to determine the synchrotron emission. From this they were able to estimate U_e/U_B. In Figure 2 of Ineson et al. (2017), they found, $E_{\mathrm{equipatition}} < E(\mathrm{lm}) < 7E_{\mathrm{equipatition}}$, in the pair plasma of the lobes, where $E_{\mathrm{equipatition}}$ is the equipartition lepto-magnetic energy. The median value is $E(\mathrm{lm}) \approx 2.4E_{\mathrm{equipatition}}$. We consider this range of possible values for the north lobe of PKS 1351-018 in the following analysis. In order for this to be robust, we comment on our description of the northern component as a lobe. Recall that the MERLIN observation with a resolution ∼50–60 mas could not detect anything, except for a point source. The VLBI *S*-band image in Figure 3 did not detect anything farther from the nucleus (within ∼30 mas of the nucleus) than the north lobe. The results of Table 2 indicate that the better *S*-band VLBI observations are consistent with minimal or no missing flux density in the image. The north lobe is therefore likely to be the furthest emission region from the nucleus. It appears to be at the end of a curving continuous jet in Figure 4. Based on the Gaussian fit in Tables 1 and 3, it is definitely wider than the jet, indicating a difference in the physical composition. One could claim that it is a knot in a continuous jet that appears to be at its terminus. This would mean that it is predominantly the hot spot in the lobe that is detected. There does not seem to be edge brightening in Figures 3 and 4 that is characteristic of the hot spot in FR II radio lobes (Fanaroff & Riley 1974). However, the lack of edge brightening could be an artifact of the imperfect (u, v) coverage and insufficient resolution. We do not think this to be the case since the north lobe seems to be significantly inflated relative to the jet. In any event, our jet analysis does not depend on this distinction. The hot spots in

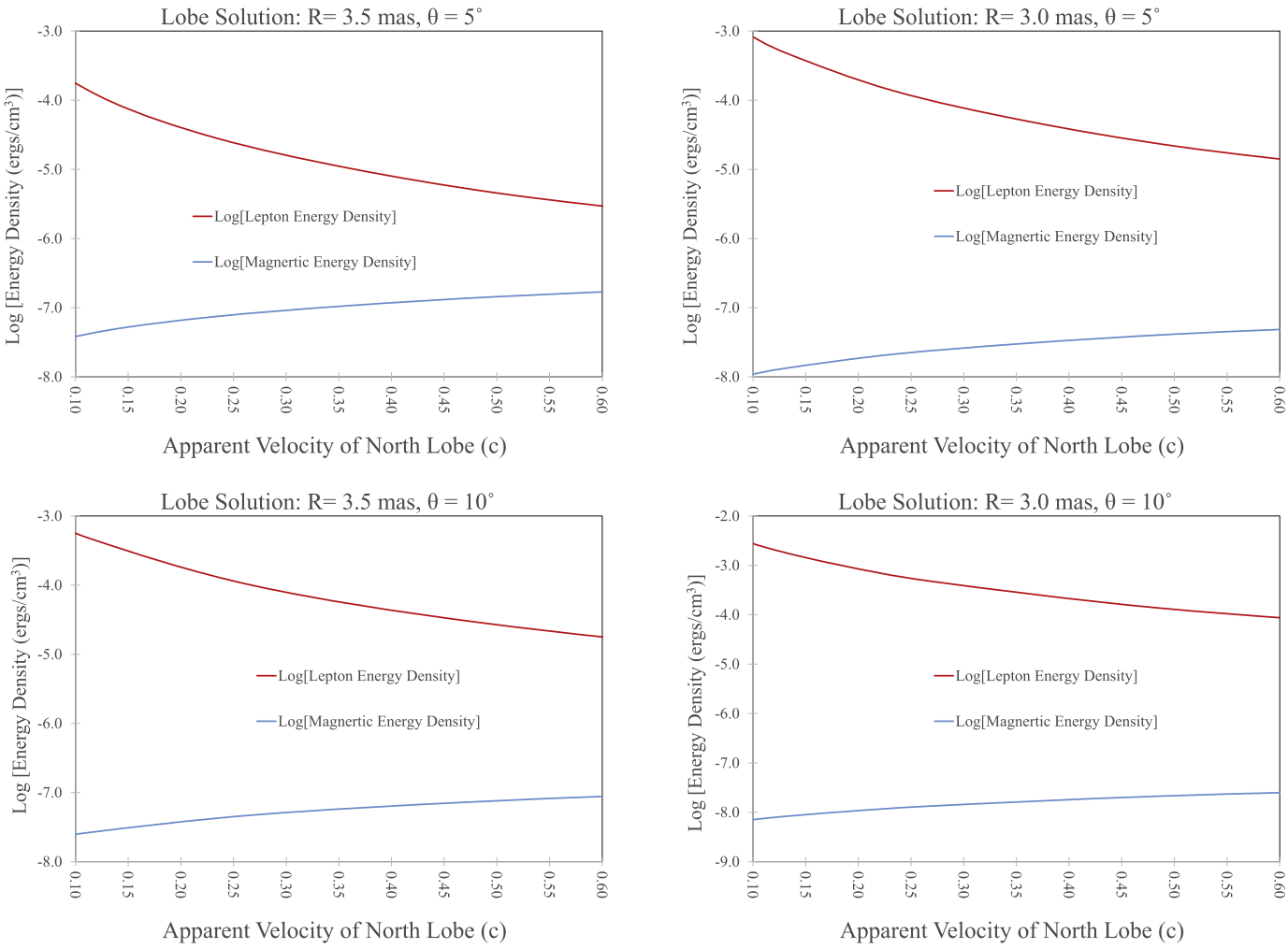

Figure 14. This figure explores a large subset of the solution space for a spherical plasmoid that radiates the fit to the north lobe (Figure 13). Based on Equations (10) and (12), we choose a rectangular subset 3.0 mas $< R <$ 3.5 mas and $5° < \theta < 10°$ and bound its behavior by looking at the four corners of the rectangle. By plotting U_e and U_B as a function of $\beta_{\rm app}$, we find no solutions that are near equipartition and obey the upper bound on $\beta_{\rm app}$ from Equation (11). The closest solution to equipartition is at $R = 3.5$ mas and $\theta = 5°$ in the upper-left panel.

FR II radio lobes and the lobe plasma deviate similarly from equipartition. The hot spots have been found to have internal energies relative to equipartition in a range very similar to the lobes (Kataoka & Stawarz 2005).

Figure 14 indicates that the larger value of R and the smaller value of θ moves the solutions closer to equipartition. Thus motivated, we look at the $R = 3.5$ mas case with $\theta < 5°$ as a possible viable region of the solution space. The first thing that we explore is the dependence of U_e and U_B on δ in the top-left-hand panel of Figure 15. It is clear that for $E_{\rm equipatition} < E({\rm lm}) < 7E_{\rm equipatition}$, $\delta \lesssim 5.5$. This is a large Doppler factor for the modest apparent velocity in Equation (11). This is explained with Equation (13) as a consequence of a small LOS.

The top-right panel of Figure 15 plots $\beta_{\rm app}$ as a function of the angle to the LOS under four different constraints, in the range $E_{\rm equipatition} < E({\rm lm}) < 7E_{\rm equipatition}$. As U_B/U_e is lowered, a larger LOS is consistent with $\beta_{\rm app} < 0.57$. Even so, the largest LOS angle in any of the plausible models is $\approx 5.8°$ for $E({\rm lm}) = 7E_{\rm equipatition}$. The bottom-left panel uses Equation (20) to plot the lepto-magnetic jet power, $Q_{\rm lm}$, as a function of the LOS angle for four cases in the range, $E_{\rm equipatition} < E({\rm lm}) < 7E_{\rm equipatition}$. The black dashed curve represents the $\beta_{\rm app} = 0.57$ upper limit implied by Figure 6. The only solutions consistent with observation are to the left of the black dashed curve. We also investigate the consequences of abandoning the $E_{\rm min} = m_e c^2$ assumption. The bottom-right panel is a plot of $Q_{\rm lm}$ as a function of the LOS angle, assuming that $E_{\rm min} = 5m_e c^2$. This value is motivated by the model of the γ-ray emission in Sahakyan et al. (2020), which has $E_{\rm min} = 2.6 m_e c^2$ in the nucleus. We intentionally went above this value in order to bound a range of plausible assumptions. However it is not clear why $E_{\rm min}$ would exceed $m_e c^2$ and is included for the sake of completeness. There is only modest variation over the entire plausible parameter range $Q_{\rm lm} \approx (5.2 \pm 3.2) \times 10^{45}$ erg s^{-1}. Note that the allowed LOS angle increases to 7.2° when $E_{\rm min} = 5m_e c^2$. The core synchrotron and inverse Compton emission (γ-ray emission) was used in Sahakyan et al. (2020) and Marcotulli et al. (2020) to estimate $Q_{\rm lm} = 2.76 \times 10^{45}$ erg s^{-1} and $Q_{\rm lm} = 4.24 \times 10^{45}$ erg s^{-1}, respectively. Remarkably, the lepto-magnetic jet power estimates on sub-parsec scales agree with our estimate $\sim$2.5 kpc (after de-projection) farther out in the north lobe. If there is a (Doppler de-boosted) counterjet, the total power of the central engine would be $Q_{\rm lm} \approx (1.04 \pm 0.64) \times 10^{46}$ erg s^{-1}.

We validate that the energy budget in the approaching jet derived from the north lobe is sufficient to support the radiation

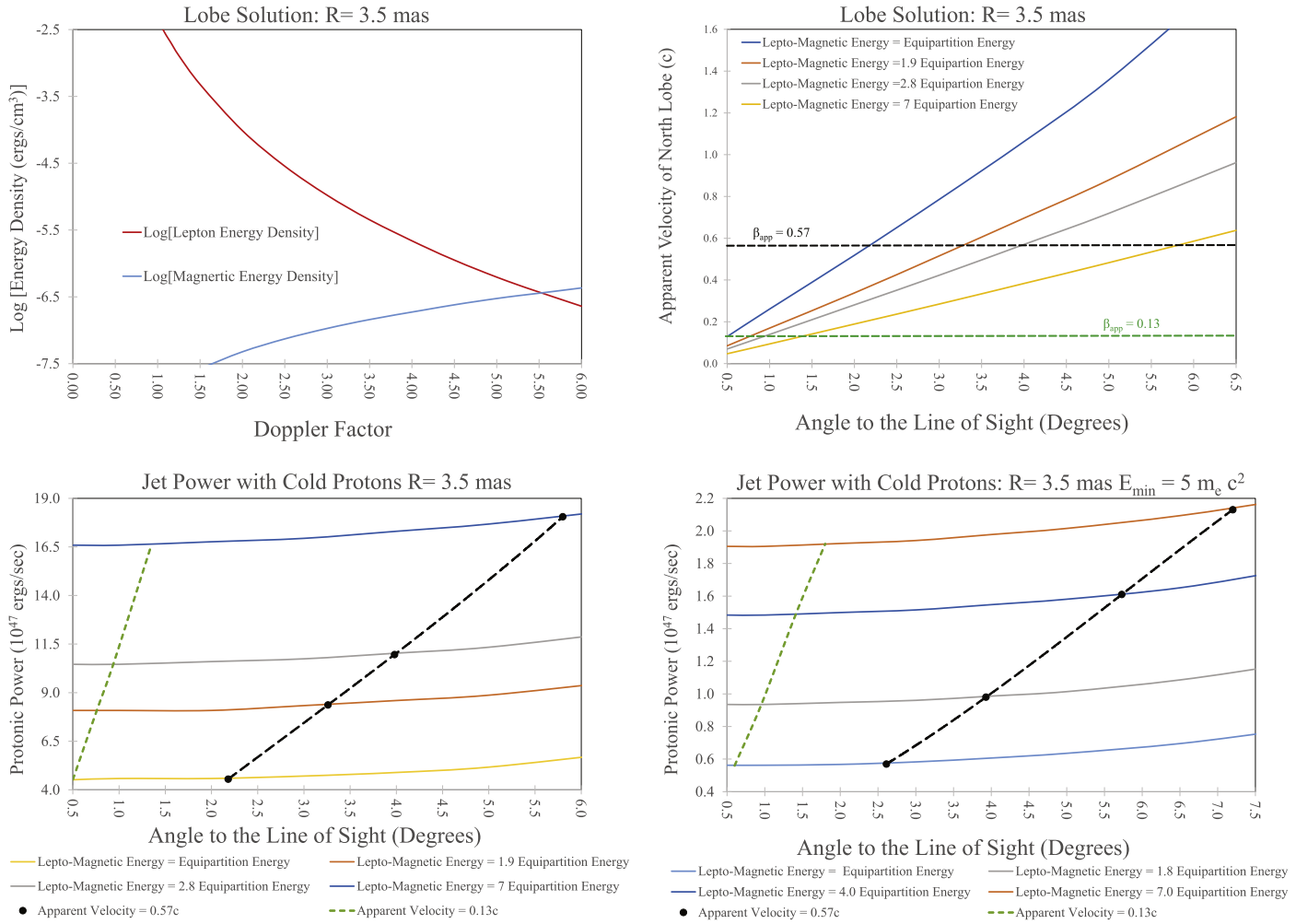

Figure 15. The figure presents plots that describe the properties of the preferred solution for the lepton-positron lobe model. The top-left panel shows the connection between the energy density of the magnetic field and the energy density of the leptons as a function of δ. Ostensibly, the plot appears to be independent of $\beta_{\rm app}$ and θ. However, as discussed earlier, that dependency is contained within the dependent variable, $\delta(\beta_{\rm app}, \theta)$. The top-right panel shows how $\beta_{\rm app}$ depends on θ for four families of solutions with energy densities consistent with the FR II energy densities found in FR II radio lobes Ineson et al. (2017). The bottom-left panel is the estimated power of the lepto-magnetic jet feeding the lobes as a function of the LOS for these same four families of solutions. Note the dashed black curve that represents the upper limit from Figure 6 of $\beta_{\rm app} < 0.57$. The only solutions consistent with this observational constraint are to the left of the dashed curve. The green dashed curve are solutions with the best-fit velocity from Figure 6. The bottom-right panel is a similar plot with the condition $E_{\rm min} = 5m_ec^2$ instead of $E_{\rm min} = m_ec^2$ as was assumed in the other three panels. The change in the estimated jet power is ≈35%.

losses. The intrinsic γ-ray luminosity, $L_\gamma(\text{intrinsic}) = \delta^{-4}L_\gamma(\text{apparent})$. From the estimated δ in the γ-ray emitting region from Sahakyan et al. (2020) and the value of δ from Marcotulli et al. (2020), we find $L_\gamma(\text{intrinsic}) = (20.47^{-4})\ 5.78 \times 10^{47}\ \text{erg s}^{-1} = 3.29 \times 10^{42}\ \text{erg s}^{-1}$ and $L_\gamma(\text{intrinsic}) = (15.4^{-4})5.78 \times 10^{47}\ \text{erg s}^{-1} = 1.03 \times 10^{43}\ \text{erg s}^{-1}$, respectively for the time averaged L_γ(apparent) from Section 6. Even if we look at the peak flare luminosity in 2016 in a 3 week bin in Figure 12, this only increases by an order of magnitude. The energy budget of the jet that is dissipated as γ-rays and the synchrotron peak is a negligible fraction of the total jet power.

We can also estimate the $P\Delta V$ work of inflating the lobe in the environment of the host galaxy. From Figure 2 of Mathews & Brighenti (2003), we get an estimate of an external pressure on the order of 1 kpc from the nucleus (where most of the lobe propagation occurs), $P_{\rm ext} \sim 10^{-10}\ \text{dyn cm}^{-2}$ if the host galaxy is a large elliptical. From the expression for the pressure, below Equation (19), the internal lobe pressures are $2 \times 10^{-7}\ \text{dyn cm}^{-2} < P < 2 \times 10^{-6}\ \text{dyn cm}^{-2}$ for the solutions in Figure 15. The north lobe is highly over-pressurized relative to the environment. Much more jet energy is required to energize the plasma in the lobe volume than is required to push the enveloping gas away as this volume inflates. We conclude that the $P\Delta V$ work of inflating the lobe is insignificant in our jet power estimates.

8.2. A Protonic North Lobe

In principle, the positive charges in the ionized lobes can be protonic matter instead of positronic matter. This was proposed by Marcotulli et al. (2020) in their model of the γ-ray emitting region. These are not thermal protons that add to the pressure, but cold protons. A significant thermal proton population in FR II radio lobes has been argued to be implausible (Croston et al. 2018). Based on Equations (16) and (18), the kinetic energy of the protons would be much larger than E(lm). The spectrum is created by electrons that radiate in the magnetic field. The spectrum is still depicted by the fit in Figure 13. However, the kinetic luminosity of the moving lobe computed from Equation (17) is much larger in Figure 16 compared to the bottom panels of Figure 15. We find no compelling reason to

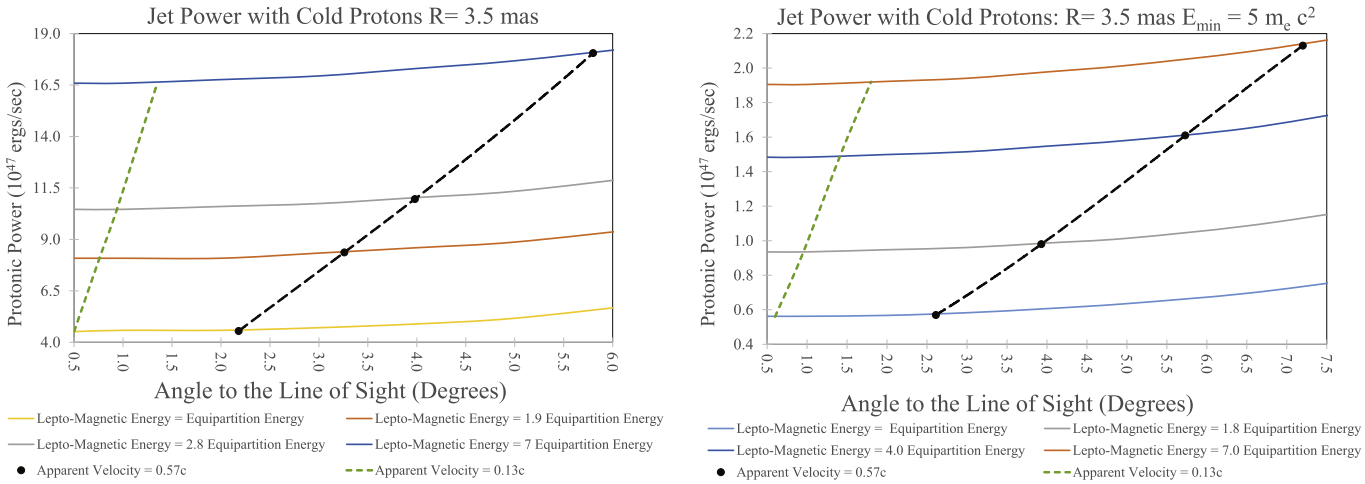

Figure 16. The jet power computed under the assumption that the positive charges are cold protons. Otherwise, the plots are identical in format to the bottom two panels of Figure 15. The allowable physical solutions exist to the left of the black dashed curves. The green dashed curve represents solutions with the apparent velocity derived from the fit to the component separation in Figure 6.

add these cold protons, but we cannot prove that this is not the case. One thing that is not encouraging is the kinetic luminosity of the protons in the lobe is an order of magnitude larger than Marcotulli et al. (2020) estimated in the γ-ray region.

9. Discussion and Concluding Remarks

The quasar, PKS 1351-018, is at the high end of the quasar synchrotron luminosity distribution, $>10^{47}$ erg s^{-1} (Section 4). The synchrotron spectrum displays very benign blazar characteristics. In particular, the radio flux density is mildly variable even at 100 GHz in the quasar rest frame. But to the contrary, there were two strong γ-ray flares in 2011 and 2016 as shown in Section 6. We explore this dichotomous behavior through various analyses in this paper. In Section 2, the $\nu_o = 5$ GHz ($\nu = 23.5$ GHz) light curve was created. Even though the variability tends to be on the same order of magnitude as the measurement uncertainty, we were able to find a flaring event in 1990 that required a relativistic outflow with a LOS $<7.1°$ to the jet. In Section 3, we studied the VLBI images at various frequencies from 1995–2020. Combined with VLA and MERLIN images, we determine that the source is very compact, confined within $\sim$15 mas. There is a conspicuous lobe-like feature to the north at the end of a jet 12 mas from the nucleus. It appears very steady in both position and flux density over 23 yr. We use these properties to constrain a physical model of the lobe in Sections 7 and 8. The kinematics of the lobe are used to estimate the jet power, $Q \approx (5.2 \pm 3.2) \times 10^{45}$ erg s^{-1}, with quite possibly a similar energy flux directed in a counterjet. The physical model is corroborated by two independent results. The jet power agrees with the jet power estimated from studies of the γ-ray flares in the nucleus ($\sim$1–3 kpc away) based on completely different assumptions and physical conditions. Furthermore, a polar LOS $<5.8°$ is required for any realistic physical model of the north lobe, a derivation that is independent of the light-curve analysis in Section 2.

We also note that there might be an interaction between the jet and the high ionization wind indicated from the spectral analysis in Section 5. The jet is very highly curved based on Tables 1, 3, and 4, even compared to most blazars (Britzen et al. 2008; Kharb et al. 2010). The curving jet is most clearly illustrated in the panel on the right of Figure 5. Based on the elongation of the nuclear Gaussian in multiple epochs the jet begins in the southwest direction in the first 0.5–0.7 mas, then it swings to the southeast at about 1.1 mas from the nucleus. Apparently, after passing through the *knot in the north jet* about 2–3 mas from the nucleus in the northeast quadrant, it ends up slightly west of north in the north lobe. The jet direction rotates $\sim$210°. Most likely, the bending is enhanced by Doppler aberration, but this does not preclude some modest intrinsic bending. In fact there needs to be some intrinsic or seed bending that is magnified by Doppler aberration. The shear layer between the jet and the denser, slower wind can decelerate the jet and possibly deflect the trajectory a few degrees. This could reduce the magnitude of the relativistic effects, thereby stabilizing the synchrotron luminosity and explain the large swing in the jet PA. This is speculative, but it does tie together three, otherwise coincidental, extreme behaviors of the source:

1. A luminous high ionization wind moving at $\sim$4000 km s^{-1} is rare in radio-loud quasars (Richards et al. 2002; Punsly 2010). Such a fast wind is rare even for luminous radio-quiet quasars (Sulentic et al. 2017).
2. The parsec scale jet trajectory bends 210°.
3. The preponderance of the enormous synchrotron flux is emitted by a region that has low variability.

We are grateful to the referee who made many useful comments that improved this work. Matt Lister provided many VLBI fits that benefited the early stages of this work and motivated the path going forward. We are grateful to Lorant Sjouwerman, Jamie Stevens, and Natasha Hurley-Walker for help and guidance with the NVAS, ATCA, and GLEAM data, respectively. Marco Berton and Matt Stevens generously provided useful JVLA data reductions. We thank Shane O'Sullivan for the 5 GHz VLBI images and fits. We were also fortunate to be helped by Narek Sahakyan, Lea Marcotulli, and Vaidehi Paliya with the high energy data. Wendy Peters generously provided us with VLITE data. Basic research in radio astronomy at the U.S. Naval Research Laboratory is supported by 6.1 Base Funding. Construction and installation of VLITE was supported by the NRL Sustainment Restoration

and Maintenance fund. The VLA is operated by the National Radio Astronomy Observatory (NRAO). We would like to thank Anita Richards of the MERLIN/VLBI National Facility for supplying the 5 GHz data. This work was supported by the National Radio Astronomy Observatory, a facility of the National Science Foundation operated under cooperative agreement by Associated Universities, Inc. This publication made use of the Astrogeo VLBI FITS image database (http://astrogeo.org/vlbi_images/) maintained by Leonid Petrov. S.F. thanks the Hungarian National Research, Development and Innovation Office (OTKA K134213) for support. A.B.P. was supported by the Russian Science Foundation grant 21-12-00241.

Appendix A
The *C*-band Data in Figures 1 and 2

Table 6
Radio Data Used in Figures 1 and 2

Date	Flux Density (mJy)	Telescope	Reference
1968 Aug 3	940 ± 47	Parkes 64 m Telescope	Wall (1972)
1980 Nov 18	880 ± 44	VLA	Perley (1982)
1986 Oct 4	940 ± 47	VLA	Drinkwater et al. (1997)
1989 Jan 14	863 ± 86	VLA	This paper
1989 Mar 30	857 ± 86	VLA	This paper
1989 May 28	878 ± 88	VLA	This paper
1989 Dec 8	834 ± 83	VLA	This paper
1990 Mar 23	854 ± 43	VLA	This paper
1990 Apr 29	868 ± 43	VLA	This paper
1990 Jul 8	987 ± 99	VLA	This paper
1990 Aug 14	917 ± 92	VLA	This paper
1990 Nov 4	1000 ± 50	VLA	This paper
1991 Jun 15	905 ± 91	VLA	This paper
1992 Nov 28	879 ± 88	VLA	This paper
1993 Jun 12	920 ± 92	VLA	This paper
1993 Sep 8	920 ± 46	VLA	This paper
1994 Jan 8	936 ± 47	VLA	This paper
1995 Sep 13	974 ± 49	VLA	This paper
1995 Dec 15	954 ± 95	MERLIN	This paper
1997 Jan 23	924 ± 92	VLA	This paper
1997 Jun 25	948 ± 95	VLA	This paper
1997 Jul 20	988 ± 99	VLA	This paper
1998 Mar 24	914 ± 91	VLA	This paper
1998 Apr 23	953 ± 53	VLA	This paper
1998 Jun 2	911 ± 46	VLA	This paper
1998 Jun 7	919 ± 46	VLA	This paper
1998 Jun 11	904 ± 45	VLA	This paper
1998 Aug 20	884 ± 88	VLA	This paper
1998 Aug 31	883 ± 88	VLA	This paper
1998 Dec 1	886 ± 44	VLA	This paper
1998 Dec 5	894 ± 89	VLA	This paper
2000 Jun 25	844 ± 84	VLA	This paper
2000 Oct 16	862 ± 43	VLA	This paper
2002 Mar 11	885 ± 88	VLA	This paper
2004 Dec 22	902 ± 90	VLA	This paper
2005 Jun 13	920 ± 46	ATCA	ATCA Calibrator Database
2007 Feb 5	952 ± 49	ATCA	ATCA Calibrator Database
2007 Feb 19	937 ± 47	ATCA	ATCA Calibrator Database
2008 May 28	952 ± 48	ATCA	ATCA Calibrator Database
2009 Feb 15	936 ± 47	ATCA	ATCA Calibrator Database
2010 Feb 13	935 ± 47	ATCA	ATCA Calibrator Database
2011 May 22	988 ± 49	ATCA	ATCA Calibrator Database
2012 Mar 18	959 ± 48	ATCA	ATCA Calibrator Database
2012 Apr 23	960 ± 48	ATCA	ATCA Calibrator Database
2012 Oct 26	945 ± 47	ATCA	ATCA Calibrator Database
2013 Feb 8	946 ± 47	ATCA	ATCA Calibrator Database
2013 May 30	960 ± 48	ATCA	ATCA Calibrator Database
2013 Sep 12	959 ± 48	ATCA	ATCA Calibrator Database
2014 Feb 1	920 ± 46	ATCA	This paper
2014 Mar 25	946 ± 47	ATCA	ATCA Calibrator Database
2015 Jun 22	888 ± 44	ATCA	This paper
2015 Ju1 11	898 ± 45	ATCA	This paper

Table 6
(Continued)

Date	Flux Density (mJy)	Telescope	Reference
2015 Oct 15	929 ± 46	ATCA	This paper
2015 Dec 9	912 ± 46	ATCA	This paper
2016 Jan 13	946 ± 47	ATCA	This paper
2016 Jan 27	927 ± 46	ATCA	ATCA Calibrator Database
2016 Feb 16	912 ± 46	ATCA	This paper
2016 Mar 5	894 ± 45	ATCA	This paper
2016 Apr 14	907 ± 45	ATCA	This paper
2016 May 8	898 ± 46	ATCA	This paper
2016 May 18	891 ± 45	ATCA	This paper
2016 Jun 8	877 ± 44	ATCA	This paper
2016 Aug 22	868 ± 43	ATCA	This paper
2016 Sep 29	880 ± 44	ATCA	This paper
2016 Nov 4	901 ± 45	ATCA	This paper
2016 Dec 3	886 ± 44	ATCA	This paper
2016 Dec 5	885 ± 44	ATCA	This paper
2017 Jan 21	865 ± 43	ATCA	This paper
2017 Feb 3	862 ± 43	ATCA	This paper
2017 Mar 2	866 ± 43	ATCA	This paper
2017 Apr 11	874 ± 44	ATCA	This paper
2017 Apr 12	873 ± 44	ATCA	ATCA Calibrator Database
2017 May 14	856 ± 43	ATCA	This paper
2017 Jun 12	876 ± 44	ATCA	ATCA Calibrator Database
2018 Oct 16	858 ± 43	ATCA	ATCA Calibrator Database
2020 Feb 22	843 ± 42	ATCA	ATCA Calibrator Database
2020 Apr 3	858 ± 43	ATCA	ATCA Calibrator Database
2020 Sep 20	836 ± 42	ATCA	ATCA Calibrator Database

Appendix B
Error Analysis

There are many VLBI observations analyzed in Section 3. The observations are quite heterogenous, spanning 33 yr. We are unable to access the visibility data for some of the observations reported in the literature. So we cannot estimate uncertainties in the Gaussian component flux density and position using the residuals of the fit to the visibility data, the post-fit rms noise, $\sigma_{\rm rms}$ (Fomalont 1999; Lee et al. 2008). Our aim is assign uncertainties to the fitted components in a uniform manner. For example, if some references in the literature assign liberal uncertainties to component positions and a conservative estimate is implemented on others, this will affect the determination of component motion in a weighted least squares fit to the trajectory. So, we are motivated to use an approximate uncertainty in the distance between the nucleus and the components of $\sim 1/5$ of the projection of the elliptical Gaussian synthesized beam FWHM along this direction (Lister et al. 2009, 2013). This can be applied uniformly to all of the observations.

The uncertainty in the component flux densities for the VLBI measurements are of two varieties. Since the core has >90% of the total flux, we note that its uncertainty is approximated as the absolute flux density calibration uncertainty of ≈10% associated with the VLBI observation (Homan et al. 2002; Pushkarev & Kovalev 2012). This approximation is applied uniformly to all the observations. There is a signal-to-noise ratio (S/N) driven uncertainty in the total flux density, S, of a component, $\sigma_{\rm tot}$, that is the dominant uncertainty for the other much weaker components (Fomalont 1999; Lee et al. 2008). In particular, $\sigma_{\rm tot} \simeq S(1+{\rm S/N})^{0.5}/{\rm S/N}$, where ${\rm S/N} = \sigma_{\rm rms}/S_{\rm peak}$ and $S_{\rm peak}$ is the peak intensity of the component. But as stated above, $\sigma_{\rm rms}$ is not known or derivable in some cases. In order to derive a uniform estimate of the uncertainty of the flux density, we computed the S/N driven uncertainty for numerous cases for which we could determine $\sigma_{\rm rms}$. This uncertainty was added in quadrature with the 10% absolute calibration uncertainty. There are three components (besides the core) that appear in our fits in Tables 1, 3 and 4. For various observations, we estimate a total uncertainty of ∼40% in the north lobe flux density, $S_{\rm north\ lobe}$, $\sigma_{\rm north\ lobe} \approx 0.4 S_{\rm north\ lobe}$. The other components are nearly point sources (S measured in mJy $\approx S_{\rm peak}$ measured in millijansky per beam) and theoretically the uncertainty should scale approximately with flux density, S, as $(\sigma_{\rm component}/S) \approx 0.4(S_{\rm north\ lobe}/S)^{0.5}$. Our uncertainty estimates verify this to be true empirically as well. Using this prescription, we can uniformly apply these approximate uncertainties to all the Gaussian brightness distribution models in this paper. None of our results in Section 8 depend strongly on the precise magnitudes of these uncertainties in flux density.

ORCID iDs

Brian Punsly https://orcid.org/0000-0002-9448-2527
Sándor Frey https://orcid.org/0000-0003-3079-1889
Paola Marziani https://orcid.org/0000-0002-6058-4912
Alexander Pushkarev https://orcid.org/0000-0002-9702-2307
Preeti Kharb https://orcid.org/0000-0003-3203-1613

References

Abdo, A. A., Ackermann, M., Ajello, M., et al. 2011, ApJL, 733, L26
Ackermann, M., Ajello, M., Baldini, L., et al. 2017, ApJL, 837, L5
Baldwin, J., Wampler, E., & Gaskell, M. 1989, ApJ, 338, 630
Becker, R., White, R. L., & Helfand, D. 1995, ApJ, 450, 595

Blundell, K., & Rawlings, S. 2000, AJ, 119, 1111
Britzen, S., Vermeulen, R. C., Campbell, R. M., et al. 2008, A&A, 484, 119
Brotherton, M. 1996, ApJS, 102, 1
Brotherton, M., Wills, B., Steidel, C., & Sargent, W. 1994, ApJ, 430, 131
Cardelli, J., Clayton, G., & Mathis, J. 1989, ApJ, 345, 245
Celotti, A., & Ghisellini, G. 2008, MNRAS, 385, 283
Clarke, T., Kassim, N., Brisken, W., et al. 2016, Proc. SPIE, 9906, 99065B
Condon, J. J., Cotton, W. D., Greisen, E. W., et al. 1998, AJ, 115, 1693
Croston, J. H., Ineson, J., & Hardcastle, M. J. 2018, MNRAS, 476, 161
Davis, S., & Laor, A. 2011, ApJ, 728, 98
de Vries, W. H., Barthel, P. D., & O'Dea, C. P. 1997, A&A, 321, 105
Diamond-Stanic, A. M., Fan, X., Brandt, W. N., et al. 2009, ApJ, 699, 782
Douglas, J., Bash, F., Bozyan, F. A., Torrence, G., & Wolfe, C. 1996, AJ, 111, 1945
Drinkwater, M., Webster, R., Francis, P., et al. 1997, MNRAS, 284, 85
Dunlop, J. S., Peacock, J. A., Savage, A., et al. 1989, MNRAS, 238, 1171
Ezeugo, J., & Ubachukwu, A. 2010, MNRAS, 408, 2256
Fanaroff, B. L., & Riley, J. M. 1974, MNRAS, 167, 31P
Fey, A. L., & Charlot, P. 2000, ApJS, 128, 17
Fomalont, E. 1999, in ASP Conf. Ser. 180, Synthesis Imaging in Radio Astronomy II, ed. G. Taylor, C. Carilli, & R. Perley (San Francisco, CA: ASP), 301
Frey, S., Gurvits, L. I., Kellermann, K. I., et al. 1997, A&A, 325, 511
Frey, S., Gurvits, L. I., Lobanov, A. P., et al. 2002, in Proc. 6th EVN Symp. New Developments in VLBI Science and Technology, ed. E. Ros et al. (Bonn: Max-Planck-Institut für Radioastronomie), 89
Ghisellini, G., Righi, C., Costamante, L., & Tavecchio, F. 2017, MNRAS, 469, 255
Ghisellini, G., Tavecchio, F., Foschini, L., et al. 2010, MNRAS, 402, 497
Ghosh, K., & Punsly, B. 2007, ApJL, 661, 139
Ginzburg, V., & Syrovatskii, S. 1965, ARA&A, 3, 297
Ginzburg, V., & Syrovatskii, S. 1969, ARA&A, 7, 375
Hardcastle, M., Evans, D., & Croston, J. 2009, MNRAS, 396, 1929
Homan, D. C., Ojha, R., Wardle, J. F. C., et al. 2002, ApJ, 568, 99
Hovatta, T., Valtaoja, E., Tornikoski, M., & Lähteenmäki, A. 2009, A&A, 498, 723
Hurley-Walker, N. 2017, arXiv:1703.06635
Ineson, J., Croston, J. H., Hardcastle, M. J., & Mingo, B. 2017, MNRAS, 467, 1586
Intema, H. T., Jagannathan, P., Mooley, K. P., & Frail, D. A. 2017, A&A, 598, A78
Kataoka, J., & Stawarz, Ł. 2005, ApJ, 622, 797
Kellermann, K. I., & Owen, F. 1988, in Galactic and Extragalactic Radio Astronomy, ed. G. L. Verschuur & K. I. Kellermann (Berlin: Springer), 577
Kellermann, K. I., & Pauliny-Toth, I. I. K. 1969, ApJL, 155, L71
Kharb, P., Lister, M. L., & Cooper, N. J. 2010, ApJ, 710, 764
Kovalev, Y. Y., Nizhelsky, N. A., Kovalev, Yu. A., et al. 1999, A&AS, 139, 545
Laor, A., Fiore, F., Elvis, M., Wilkes, B., & McDowell, J. 1997, ApJ, 477, 93
Lawrence, A., Warren, S., Almaini, O., et al. 2007, MNRAS, 379, 1599
Lee, S.-S., Lobanov, A., Krichbaum, T. P., et al. 2008, AJ, 136, 159
Li, S., Xia, Z.-Q., Liang, Y.-F., Liao, N.-H., & Fan, Y.-Z. 2018, ApJ, 853, 159
Lind, K., & Blandford, R. 1985, ApJ, 295, 358
Lister, M. L., Aller, M. F., Aller, H. D., et al. 2013, AJ, 146, 120
Lister, M. L., Cohen, M., Homan, D., et al. 2009, AJ, 138, 1874
Marcotulli, L., Paliya, V., Ajello, M., et al. 2020, ApJ, 889, 164
Marziani, P., Sulentic, J., Negrete, A., et al. 2010, MNRAS, 409, 1033
Mathews, W., & Brighenti, F. 2003, ARA&A, 41, 191
Mattox, J. R., Bertsch, D. L., Chiang, J., et al. 1996, ApJ, 461, 396
Moffet, A. 1975, in Stars and Stellar Systems. IX. Galaxies and the Universe, ed. A. Sandage, M. Sandage, & J. Kristan (Chicago, IL: Chicago Univ. Press), 211
Murphy, T., Sadler, E., Ekers, R., et al. 2010, MNRAS, 402, 2403
Murray, N., Chiang, J., Grossman, S., & Voit, G. 1995, ApJ, 451, 498
Nandra, K., George, I. M., Mushotzky, R. F., Turner, T. J., & Yaqoob, T. 1997, ApJ, 476, 30
Neff, S. G., & Hutchings, J. B. 1990, AJ, 100, 1441
Netzer, H., & Marziani, P. 2010, ApJ, 724, 318
O'Dea, C. P., Baum, S. A., & Stanghellini, C. 1991, ApJ, 380, 66
Osmer, P. S., Porter, A. C., & Green, R. F. 1994, ApJ, 436, 678
O'Sullivan, S., Gabudza, D., & Gurvits, L. 2011, MNRAS, 415, 3049
Perley, R. 1982, AJ, 87, 859
Perley, R., & Butler, B. 2013, ApJS, 204, 19
Petrov, L. 2021, AJ, 161, 14
Petrov, L., Gordon, D., Gipson, J., et al. 2009, JGeod, 83, 859
Polisensky, E., Lane, W. M., Hyman, S. D., et al. 2016, ApJ, 832, 60
Punsly, B. 1995, AJ, 109, 1555
Punsly, B. 2008, Black Hole Gravitohydromagnetics (2nd ed.; New York: Springer)
Punsly, B. 2010, ApJ, 713, 232
Punsly, B. 2012, ApJ, 746, 91
Punsly, B. 2019, ApJL, 871, L34
Punsly, B., Hill, G. J., Marziani, P., et al. 2020, ApJ, 898, 169
Punsly, B., Marziani, P., Zhang, S., Muzahid, S., & O'Dea, C. 2016, ApJ, 830, 104
Pushkarev, A., & Kovalev, Y. 2012, A&A, 544, 34
Readhead, A. 1994, ApJ, 426, 51
Reed, B. 1989, AmJPh, 57, 642
Rees, M. J. 1966, Natur, 211, 468
Reynolds, C., Punsly, B., Kharb, P., O'Dea, C., & Wrobel, J. 2009, ApJ, 706, 851
Reynolds, C., Punsly, B., Miniutti, G., O'Dea, C., & Hurley-Walker, N. 2020, ApJ, 891, 59
Richards, G., Vanden Berk, D., Reichard, T., et al. 2002, AJ, 124, 1
Sahakyan, N., Israyelyan, D., Harutyunyan, G., Khachatryan, M., & Gasparyan, S. 2020, MNRAS, 498, 2594
Spoelstra, T. A. T., Patnaik, A. R., & Gopal-Krishna 1985, A&A, 152, 38
Steppe, H., Jeyakumar, S., Saikia, D., & Salter, C. 1995, A&AS, 113, 409
Sulentic, J., del Olmo, A., Marziani, P., et al. 2017, A&A, 608, 122
Sulentic, J., Marziani, P., & Dultzin-Hacyan, D. 2000, ARA&A, 38, 521
Telfer, R., Zheng, W., Kriss, G., & Davidsen, A. 2002, ApJ, 565, 773
Tornikoski, M., Jussila, I., Johansson, P., Lainela, M., & Valtaoja, E. 2001, AJ, 121, 1306
Valtaoja, E., Lähteenmäki, A., Teräsranta, H., & Lainela, M. 1999, ApJS, 120, 95
van der Laan, H. 1966, Natur, 211, 1131
Wall, J. 1972, AuJPA, 24, 1
Wayth, R. B., Lenc, E., Bell, M. E., et al. 2015, PASA, 32, e025
Willott, C., Rawlings, S., Blundell, K., & Lacy, M. 1999, MNRAS, 309, 1017
Wright, E. L. 2006, PASP, 118, 1711
Zheng, W., Kriss, G., Telfer, R., et al. 1997, ApJ, 475, 469